

Contents lists available at ScienceDirect

Journal of the Mechanics and Physics of Solids

journal homepage: www.elsevier.com/locate/jmps





Hybrid discrete-continuum modeling of shear localization in granular media

Peter Yichen Chen ^a, Maytee Chantharayukhonthorn ^b, Yonghao Yue ^c, Eitan Grinspun ^{a,d,*}, Ken Kamrin ^{b,*}

- ^a Columbia University, 116th St & Broadway, New York, NY 10027, USA
- ^b Massachusetts Institute of Technology, 77 Massachusetts Ave, Cambridge, MA, 02139, USA
- ^c Aoyama Gakuin University, O-525, Fuchinobe 5-10-1, Chuo-ku, Sagamihara, Kanagawa, 252-5258, Japan
- ^d University of Toronto, 40 St. George Street, Room 4283, Toronto, ON M5S 2E4, Canada

ARTICLE INFO

Keywords: Shear localization Finite size effects Mesh dependence Discrete-continuum coupling Multiscale modeling Granular material

ABSTRACT

Shear localization is a frequent feature of granular materials. While the discrete element method can properly simulate such a phenomenon as long as the grain representation is accurate, it is computationally intractable when there are a large number of grains. The continuum-based finite element method is computationally tractable, yet struggles to capture many grain-scale effects, e.g., shear band thickness, because of mesh dependence, unless the constitutive model has a length scale. We propose a hybrid discrete-continuum technique that combines the speed of the continuum method with the grain-scale accuracy of the discrete method. In the case of shear localization problems, we start the simulation using the continuum-based material point method. As the simulation evolves, we monitor an adaptation oracle to identify the onset of shear bands and faithfully enrich the macroscopic continuum shear bands into the microscopicscale grains using the discrete element method. Our algorithm then simulates the shear band region with the discrete method while continuing to simulate the rest of the domain with the continuum method so that the computational cost remains significantly cheaper than a purely discrete solution. We validate our technique in planar shear, triaxial compression, and plate indentation tests for both dry and cohesive granular media. Our method is as accurate as a purely discrete simulation but over 100 times faster than a discrete simulation that would require tens of millions of grains.

1. Introduction

Granular material is known for its characteristic multiphase and multiscale nature (Jaeger et al., 1996). It can exhibit gaseous, liquid, and solid-like behavior simultaneously. The transitional behavior from the fluid to solid phase of granular flow shows both micro-scale discrete and macro-scale continuum attributes.

One specific feature that exhibits a strong multiscale nature is shear localization (also known as shear banding), where intensive shear strain localizes into thin regions (Mühlhaus and Vardoulakis, 1987; Mandl et al., 1977). On the one hand, shear banding is no different from typical continuum shear flow where the material undergoes shear strain while resisting a shear stress. On the other hand, shear banding displays strong discrete characteristics in that the size of shear features is influenced directly by the grain size (Kamrin, 2019; Bocquet et al., 2001; Han and Drescher, 1993; Gu et al., 2014; Oda and Kazama, 1998; Hu and Molinari, 2004).

E-mail addresses: eitan@cs.toronto.edu (E. Grinspun), kkamrin@mit.edu (K. Kamrin).

^{*} Corresponding authors.

In fact, depending on the underlying discrete grains, the shear band thickness of geological materials occurs across vastly different sizes (Daub and Carlson, 2010): from micrometer scale ($O(10^{-6})$) (Beeler et al., 1996) to millimeter scale ($O(10^{-3})$) (Chambon et al., 2006). In terms of the median grain size (D_{50}), shear band thickness can vary from 10 to 30 D_{50} (Kuhn, 2017; Roscoe, 1970; Finno et al., 1997; Vardoulakis, 1998). Shear localization often precipitates further material failure and damage, even leading to tectonic earthquakes (Towhata, 2008). It is thereby crucial to understand shear banding. Theoretical analysis has been developed to model shear banding as a bifurcation problem (Rudnicki and Rice, 1975; Rice, 1975; Mehrabadi and Cowin, 1978; Anand and Spitzig, 1980; Bigoni and Hueckel, 1991). Quantitative analysis of shear banding has also been conducted through computational modeling, which typically falls into two categories: the discrete approach and the continuum approach.

The Discrete Element Method (DEM) models each individual grain explicitly as a stiff elastic body with frictional contact (Cundall and Strack, 1979). Since the discrete approach models granular material in its fundamental scale, it captures both the continuum and discrete nature of the shear band by default, including any nonlocal and rate-dependent effects. The discrete approach has long been used for shear band simulations (Bardet and Proubet, 1991; Cundall, 1989; Bardet and Proubet, 1992; Iwashita and Oda, 1998, 2000; Oda and Iwashita, 2000) and has recently been shown to be able to simulate shear banding with unprecedented quantitative accuracy (Kawamoto et al., 2018). In fact, it is often considered the "gold standard" and is used as a ground-truth validation for other models (Rycroft et al., 2009). Unfortunately, accuracy does come with a caveat: the computational cost of the discrete method for real-world applications can easily become intractable due to the need to model an enormous number of individual grains.

The continuum approach is a computationally more efficient solution. With the continuum approach, an elastoplastic framework is usually solved with the Finite Element Method (FEM), which has significantly fewer degrees of freedom than the discrete approach. While the continuum approach has been shown to capture shear banding qualitatively, its accuracy depends highly on the underlying elastoplastic framework. The classic athermal rate-independent plasticity models are usually local in nature and lack an intrinsic characteristic length scale, which is necessary to capture any discrete size characteristics (Belytschko et al., 1988). It is therefore not a surprise that these models do not yield a finite size shear band thickness. As a result, in the FEM implementation of these models (Anand and Gu, 2000; Pietruszczak and Mroz, 1981), the thickness of the simulated band depends on the element size, converging to an erroneous band of zero thickness under refinement. Such mesh dependence also leads to numerical softening in the post-localization regime.

Nonlocal models have been developed to regularize mesh dependence by either explicitly or implicitly introducing a characteristic length scale. Nonlocal models for shear band modeling typically fall into one of the three categories: direct spatial averaging (Eringen, 1981; Bažant and Lin, 1988; Bažant et al., 1984; Belytschko et al., 1986; Chen et al., 2000), gradient theory (Yang and Misra, 2012; Engelen et al., 2003; De Borst and Mühlhaus, 1992; De Borst et al., 1995; Mühlhaus and Alfantis, 1991; Aifantis, 1984; Borst et al., 1993; Sluys et al., 1993; Chang et al., 2002), and micropolar theory (Eringen, 1966; Alshibli et al., 2006; Alsaleh et al., 2006). In certain applications, viscoplasticity (Needleman, 1988; Sluys and De Borst, 1992; Nemes and Speciel, 1996) and thermal-mechanical coupling (Lemonds and Needleman, 1986; LeMonds and Needleman, 1986; Semnani et al., 2016; Batra and Kim, 1991) are also sufficient conditions for mesh dependence regularization. While nonlocal models offer significant improvements over local models in the modeling of shear localization, more study is needed to assess how quantitatively they predict shear band properties such as thicknesses across a variety of loading conditions and geometries (Engelen et al., 2006; Poh et al., 2011; Anand et al., 2012).

In addition to the requirements for nonlocal treatments, the continuum model often requires an empirical phenomenological law to evolve plastic internal variables to correctly capture softening and dilation observed in shear localization. Yet, these empirical models can break down in flow cases different from the ones they were originally calibrated for. For example, a relation fitted from axisymmetric conditions might be inaccurate under plane strain conditions (Tu et al., 2009).

1.1. Hybrid discrete-continuum simulation

The *concurrent* multiscale methods combine the discrete approach with the continuum approach. These multiscale methods typically employ the fine-scale, accurate-yet-slow discrete simulation inside the "hot zone," where high fidelity is needed, while simultaneously using coarse-scale, fast-yet-less-precise continuum-based simulation outside the hot zone, where continuum modeling's accuracy is sufficient (Dhia, 1998; Tadmor et al., 1996b,a; Wellmann and Wriggers, 2012; Ghareeb and Elbanna, 2020; Anciaux et al., 2018; Hodapp et al., 2018; Cho et al., 2018; Shilkrot et al., 2004; Wallin et al., 2008; Yan et al., 2010). With this approach, not only does the computational cost become relatively manageable but the simulation often remains as accurate as the purely discrete approach. In addition, one does not need to supply a specialized continuum model that is designed for the particular phenomenon of interest since the simulation transitions to the discrete model whenever the continuum model reaches its modeling limits.

One particular concurrent multiscale method is the hybrid discrete-continuum framework proposed by Yue et al. (2018) to model granular flow surface details. They utilize a classic rate-independent continuum model to simulate the internal bulk and adopt a DEM model to capture details near free surfaces and boundaries, thereby achieving a seven-times speedup compared to a purely discrete treatment while capturing nuances near the system boundaries such as size effects due to small openings, non-trivial boundary sliding behaviors, and ballistic particle fly-away effects.

Building on the work of Yue et al. (2018), we present a hybrid discrete-continuum solution to shear localization problems, where we employ fine-scale discrete simulations inside the shear band and use coarse-scale continuum-based simulations outside the shear band. Specifically, in order to dynamically decompose the domain into a discrete zone and a continuum zone, we design an "oracle algorithm" that accurately identifies the formation of persistent shear bands in an arbitrary continuum simulation by monitoring the strain rate and its gradients. We then replace the shear band in the continuum simulation with grains simulated by the discrete

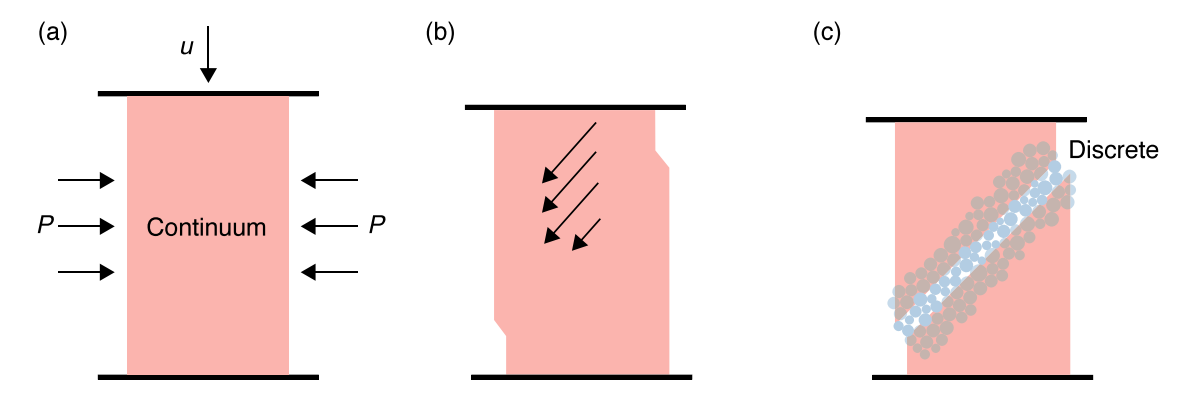


Fig. 1. A schematic illustration of the hybrid pipeline: (a) We begin the simulation in a full continuum fashion. (b) As the simulation evolves, we detect whether a continuum shear band has formed. (c) If a persistent shear band forms, we swap out the continuum shear band with discrete grains. The simulation proceeds with the discrete grains simulating the shear band and the continuum modeling the rest of the domain. An overlapping region between the discrete region and the continuum region is maintained so that the two regions are coupled.

approach. These added grains are carefully prepared through kinematic training and pre-banding in an effort to match the stress and internal state variables of the continuum shear band that they replace. After replacement, the hybrid simulation is integrated through the coupling approach of Yue et al. (2018). The proposed hybrid shear localization simulation technique requires neither nonlocal plasticity models nor empirical evolution of plastic internal variables; the method works for different phenomena with the same formulation and continuum model. We validate our approach by showing agreement between the hybrid simulation and discrete simulation in three different settings: planar shear, triaxial compression, and plate indentation. Unlike the pure continuum approach, the hybrid approach accurately captures the shear band thickness and the characteristic softening. Under large-scale scenarios that require tens of millions of discrete grains, our method offers more than a 100 times speedup over the purely discrete simulation. A schematic illustration of the algorithm is shown in Fig. 1.

Note that unlike the previous bridging-scale type of the concurrent multiscale approach (Liu et al., 2004; Qian et al., 2004; Liu et al., 2006; Qian et al., 2008; Davydov et al., 2014; Wagner and Liu, 2003) that pre-determines the partition of the discrete region and the continuum region before the start of the simulation, our approach determines the partition on-the-fly and introduces the costly discrete simulation only when a persistent shear band appears, thereby saving unnecessary computational costs. At the same time, our online partition approach offers the potential to model cases where multiple shear bands emerge and vanish at different times, e.g., due to sudden boundary condition changes. To support online partitioning, we develop a shear band detection scheme as well as a method for converting continuum to discrete representations.

While we adopt the concurrent multiscale approach, the *hierarchical* multiscale framework (Fish, 2013) has also been popular in modeling shear localization (Tu et al., 2009; Andrade and Tu, 2009; Chen, 2011; Andrade et al., 2011; Guo and Zhao, 2014, 2016b,a; Liu et al., 2016). Within the hierarchical multiscale framework, phenomenological plasticity is replaced by unit cell discrete simulations. Given a high-level continuum strain increment, the corresponding stress (Liu et al., 2016) or plastic internal variables (Andrade et al., 2011) can be computed through a low-level discrete simulation instead of phenomenological constitutive laws and then passed back to the high-level continuum simulation. Though free from an empirical constitutive relationship, hierarchical multiscale methods still experience mesh dependence unless nonlocal efforts are accounted for. Nonlocal treatments then require a priori knowledge of the location, orientation, and/or thickness of the shear band, e.g., through either physical experiments or full-size discrete simulations. By contrast, our proposed hybrid discrete-continuum multiscale framework is mesh-independent by design, with no need for explicit nonlocal treatment or prior information on the shear band.

2. Hybrid components: from stiff elastic body dynamics to solid mechanics

We begin detailing the hybrid simulation system by first documenting the individual components of the system: namely, discrete modeling based on stiff elastic body dynamics and continuum modeling based on solid continuum mechanics.

2.1. Discrete modeling

Typically, there are two distinct approaches to discrete modeling: the "soft" approach based on penalties of grain overlapping (Cundall and Strack, 1979) and the "hard" approach where grain interactions are solved as hard constraints (Moreau, 1988). We adopt the soft approach and follow Cundall and Strack (1979) as well as Yue et al. (2018) by modeling individual grains explicitly as 2D circular stiff elastic bodies (though particles need not be round in the methodology). Here we summarize the major points of the model and refer to the original papers for details.

 Table 1

 Parameters in the discrete simulation. The grain diameters follow a normal distribution.

Parameter	Value	Unit
k_n	1772093.8	N/m
γ_n	7.0	N·s/m
k_{t}	886046.9	N/m
γ_t	7.0	N·s/m
μ	0.5	
dt	5.0×10^{-7}	S
Mean grain diameter	1.0×10^{-3}	m
Standard deviation of grain diameters	8.0×10^{-5}	m
Density	2.53×10^{3}	kg/m ³

Each grain's configuration is parameterized by three degrees of freedom: two for the location x and one for the orientation θ . Assuming the grain has mass m and moment of inertia I, the dynamics of a stiff elastic body are then described by

$$\frac{d}{dt} \begin{pmatrix} \mathbf{x} \\ \theta \\ \dot{\mathbf{x}} \\ \dot{\theta} \end{pmatrix} = \begin{pmatrix} \dot{\mathbf{x}} \\ \dot{\theta} \\ f/m \\ \Gamma/I \end{pmatrix}, \tag{1}$$

where f contains all the forces, including external forces, acting on the grain and Γ is the corresponding torque.

To model frictional forces among discrete grains, we follow Cundall and Strack (1979) by adopting a linear contact model using Coulomb's friction law with viscous damping. The normal force is defined as $f_n = k_n dn - \gamma_n v_n$, where d is the penetration depth at the contact, n is the contact normal, k_n is the normal contact stiffness constant, v_n is the relative velocity projected into the normal direction, and γ_n is the normal damping coefficient. The tangential frictional force is defined as $f_t = k_t \Delta s - \gamma_t v_t$, where k_t is the tangential contact stiffness, Δs is the tangential anchor spring, γ_t is the tangential damping coefficient, and v_t is the relative velocity projected into the tangent direction. At the end of each time step, Δs is projected to respect the Coulomb's constraint $|f_t| \le \mu |f_n|$, where μ is the coefficient of Coulomb's friction.

To model cohesion, we augment the linear contact model by Cundall and Strack (1979) with two linear cohesion terms: e_n and e_t . In the normal direction, $f_n = k_n dn - \gamma_n v_n$ is now also activated during tension as long as $k_n d < e_n$ is satisfied (Jiang et al., 2005, 2007). In the tangential direction, the Coulomb's constraint now becomes $|f_t| \le \mu |f_n| + e_t$. With this model we can effectively model cohesive bonds, wherein those bonds are only active if previous contact has occurred. The grains then must undergo sufficient separation in order to break this bond.

The parameters used in the model are listed in Table 1. We choose k_n 's value so that it gives us quasi-rigid behavior while still keeping the computational cost feasible. Since k_t , γ_n , and γ_t have little effect on dense granular flow (Da Cruz et al., 2005), we choose them using the heuristics of Kamrin and Koval (2014): $k_t/k_n = 0.5$, $\gamma_n = \gamma_t$, and e = 0.1, where e is the coefficient of restitution. The coefficient e is related to the damping coefficient through $\gamma_n = -2 \ln e \sqrt{m k_n/(\pi^2 + \ln^2 e)}$, where m is the mean mass of a grain. The time step dt is chosen to be $\tau/100$ where $\tau = \pi/\sqrt{2k_n/m} - (\gamma_n/m)^2$ is the duration of an impact event.

2.2. Continuum modeling

We adopt a generic elastoplastic framework for the continuum model. While there are a variety of granular flow models, we adopt a simple, local, dilatant, and rate-dependent model. Our motivation is that the continuum model in the hybridization framework has to be robust enough to develop shear localization and capture essential granular flow features but no more than that. In particular, it does not need to provide the exact thickness of the shear band since the hybridization process itself will provide the high fidelity simulation of the shear band.

The evolution of the continuum is governed by conservation of momentum

$$\rho \frac{Dv}{Dt} = \nabla \cdot \boldsymbol{\sigma} + \boldsymbol{f}_{ext} \tag{2}$$

and conservation of mass

$$\frac{D\rho}{Dt} + \rho \nabla \cdot \mathbf{v} = 0,\tag{3}$$

where ρ is the mass density, v is the continuum velocity, σ is the Cauchy stress tensor, $\frac{D}{Dt}$ is the material derivative, and f_{ext} is the total external force.

For elastoplasticity, we employ a multiplicative decomposition of the deformation gradient $F = F^e F^p$, where F^e and F^p denote the elastic and the plastic parts of the deformation gradient, respectively. The left Cauchy-Green strain is denoted by $\mathbf{b} = F F^T$. Its elastic part is $\mathbf{b}^e = F^e F^{eT}$.

For elastic response, we use the nonlinear hyperelastic Hencky material model to facilitate easy numerical implementation of plastic projection (Hencky, 1933; de Souza Neto et al., 2011). Let $e^e = \frac{1}{2} \ln b^e$ be the elastic part of the Eulerian logarithmic strain

Table 2
Parameters in the continuum MPM simulation.

Parameter	Value	Unit
K	630	MPa
G	460	MPa
ϕ_{cs}	0.27	
$oldsymbol{\phi}_{cs} \ oldsymbol{\Phi}_{cs}$	81.5%	
X	7	
ξ	0.01	

 $\epsilon = \frac{1}{2} \ln \mathbf{b}$ and $\epsilon^p = \epsilon - \epsilon^e$ be the plastic part. The elastic strain ϵ^e consists of a volumetric part $\epsilon^e_v = \text{tr}[\epsilon^e]$ and a deviatoric part $\epsilon^e_d = \epsilon^e - \frac{1}{2}\epsilon^e_v \mathbf{I}$. Then the elastic strain and stress relationship is defined linearly (with respect to ϵ^e) by

$$\tau = K \epsilon_e^{\rho} I + 2G \epsilon_e^{\rho}, \tag{4}$$

where $\tau = J\sigma$ is the Kirchhoff stress, $J = \det F$, K is the bulk modulus, and G is the shear modulus. We calibrate these elasticity parameters to the discrete model. To obtain the bulk modulus K needed for the continuum simulation, we conduct isotropic compression on the discrete specimen. To obtain the shear modulus G, we bypass the direct simple shear test due to the difficulty of preventing grains from sliding against each other, i.e., entering the plastic regime. Instead, we conduct uniaxial compression on the discrete specimen to get the P-wave modulus M and compute G from G = M - K (equivalent of $G = \frac{3}{4}(M - K)$ in 3D).

For plasticity, we use a two-invariant, cohesive Drucker-Prager model (Drucker and Prager, 1952)

Plastic yield function:
$$f = \sqrt{J_2(s)} + \eta p - \zeta c,$$
 (5)

Plastic flow potential:
$$g = \sqrt{J_2(s)} + \bar{\eta}p$$
, (6)

where $p = \frac{1}{2} \text{tr}[\tau]$ is the pressure, $J_2 = \frac{1}{2}s$: s, $s = \tau - pI$ is the deviatoric part of the Kirchhoff stress, and c represents cohesion. Other parameters η , $\bar{\eta}$, and ζ are defined through the friction angle and the dilation angle, $\eta = \sin \phi$, $\bar{\eta} = \sin \psi$, $\zeta = \cos \phi$ in accordance with the 2D Mohr-Coulomb criterion.

When $f \le 0$, the material behaves elastically. When f > 0, however, the material undergoes plastic deformation. The plastic strain rate is defined as

$$\dot{\boldsymbol{\epsilon}}^p = \dot{\lambda} \frac{\partial g}{\partial \tau} = \dot{\lambda} \left(\frac{1}{2\sqrt{J_2}} s + \frac{\bar{\eta}}{2} \boldsymbol{I} \right),$$

where $\dot{\lambda}$ is the magnitude chosen such that the consistency condition $\dot{f}=0$ from the plastic flow's Kuhn-Tucker conditions is satisfied and $\frac{\partial g}{\partial \tau}$ is the direction. Note that $\mathrm{tr}[\dot{e}^p]=\dot{\lambda}\mathrm{tr}[\frac{\bar{\eta}}{2}I]=\dot{\lambda}\bar{\eta}$, due to the deviatoric nature of s. Therefore, if the dilation angle $\psi>0$ and $\bar{\eta}=\sin\psi>0$, we have $\mathrm{tr}[\dot{e}^p]>0$, which leads to volume gain. Alternatively, if the dilation angle $\psi<0$ and $\bar{\eta}=\sin\psi<0$, we have $\mathrm{tr}[\dot{e}^p]<0$, which leads to volume loss.

The remaining continuum modeling ingredient is the hardening/softening behavior. Softening is crucial for the formation of shear bands; we therefore adopt a packing-fraction based treatment of softening. In particular, we employ the critical state plasticity model described in Wood (1990) and Askari and Kamrin (2016). This model states that the friction angle and the dilation angle are associated through $\tan \phi = \tan \phi_{cs} + \tan \psi$. Instead of constant dilation and friction angles, a dilation angle model based on the packing fraction Φ can be adopted. A straightforward one is $\tan \psi = (\Phi - \Phi_{cs}) \chi$, where Φ_{cs} is the critical packing fraction and χ is a scaling constant. Combined with critical state plasticity, we have

$$\tan \phi = \tan \phi_{cs} + (\boldsymbol{\Phi} - \boldsymbol{\Phi}_{cs}) \chi. \tag{7}$$

Thus, if the packing fraction is larger than the critical packing fraction, we have a positive dilation angle, i.e., volume gain, and the friction angle is larger than the critical friction angle. Alternatively, if the packing fraction is smaller than the critical packing fraction, we have a negative dilation angle, i.e., volume loss, and the friction angle is smaller than the critical friction angle. To describe the evolution of the packing fraction, a simple logistic differential equation (Weisstein, 2003) can be used:

$$\frac{d\boldsymbol{\Phi}}{dt} = -\left(\boldsymbol{\Phi} - \boldsymbol{\Phi}_{cs}\right)\boldsymbol{\Phi}\boldsymbol{\xi}\|\dot{\boldsymbol{\epsilon}}^p\|. \tag{8}$$

Based on this relationship, the packing fraction Φ smoothly grows/decreases towards the critical packing fraction with a rate depending on the plastic deformation rate and a dimensionless scaling parameter ξ . We calibrate these plasticity parameters from a single simple shear test by fitting the continuum stress-strain curve to its discrete counterpart. The exact values of the continuum model parameters are listed in Table 2.

2.2.1. Discretization through the material point method (MPM)

We discretize the continuum model through MPM (Sulsky et al., 1995), building on other works of MPM simulation of granular media (Bardenhagen et al., 2000; Andersen and Andersen, 2010; Abe et al., 2013; Mast et al., 2015; Dunatunga and Kamrin, 2015, 2017; Kiriyama, 2016; Daviet and Bertails-Descoubes, 2016; Klár et al., 2016; Tampubolon et al., 2017; Gao et al., 2018; Liu and Sun, 2019; Jiang et al., 2019; Liu and Sun, 2020). Recently MPM has also been adopted in the hierarchical multiscale method for

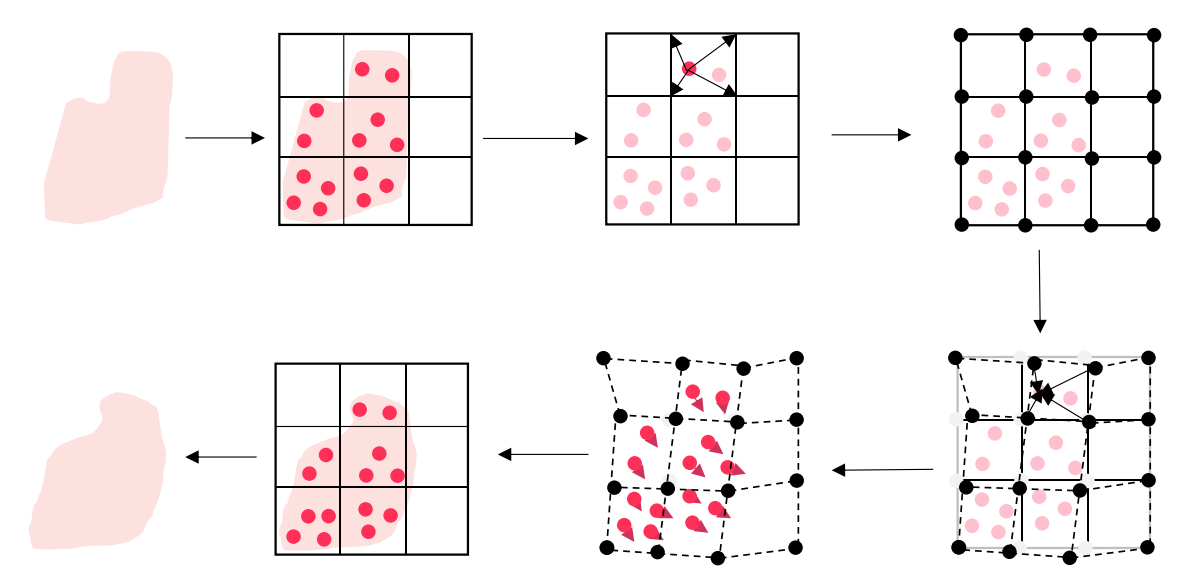


Fig. 2. MPM adopts a dual-representation of the continuum through the particles and the grid. The particles are used for advection while the grid facilitates force computation. Information is transferred between the particle view and the grid view at every time step through basis functions. MPM naturally handles large deformation, which is a key feature of granular flow.

granular media (Liu et al., 2017; Liang and Zhao, 2019). MPM's advantage compared with traditional FEM is its ability to simulate large deformation accurately and efficiently. The MPM framework employs a dual-representation of the continuum through both a grid and Lagrangian material point particles (Fig. 2). The grid allows for accurate force integration while the particles facilitate advection with large deformation. We adopt an explicit MPM integrator with a return-mapping style treatment of plasticity. We refer to the work of Yue et al. (2015, 2018) for MPM implementation details and the approach of de Souza Neto et al. (2011) for return mapping details.

3. Hybrid oracle

Two ingredients are needed to transform a purely continuum MPM shear band simulation into a hybrid shear band simulation: a partition scheme and an enrichment routine. In this section, we will detail the hybrid oracle that partitions the domain into discrete regions and continuum regions. In the subsequent section, we will discuss the enrichment routine that swaps the original continuum region with discrete grains once a partition is decided.

In the case of domain partitioning, there are typically two approaches: the Lagrangian approach and the Eulerian approach. The Lagrangian approach partitions the domain in the reference (material) space while the Eulerian approach partitions the domain in the current (deformed) space. The benefit of the Lagrangian approach is its simplicity because it is effectively a preprocessing method that decides the partition before the start of the simulation. However, its advantage is also its weakness, since we need prior knowledge of the partition, which for our work is the location of the shear band. Previous hierarchical multiscale methods have adopted this prescribed localization approach (Andrade and Tu, 2009). We take the more involved Eulerian approach that partitions the domain on the fly. The benefit of the Eulerian approach is that no prior information on the partition is needed. A key ingredient of the Eulerian approach is the ability to discern the location of the shear band during the simulation. The critical state plasticity continuum MPM simulation introduced in the previous section forms a shear band at roughly the right location and time, even though it cannot correctly deliver the exact thickness or other details of the shear band after initialization, as shown in Figs. 11, 18 and 24.

To precisely determine the shear band's location in the continuum simulation, we need to focus on certain continuum fields and set a criterion for a region to be considered inside a shear band. Previous work on adaptive mesh refinement simulation of shear localization offers us many insights on how to choose such a field. One of the early works on adaptive FEM treatment of shear localization was written by Ortiz and Quigley IV (1991), where the magnitude of continuum velocity v serves as the threshold field that decides the shear band location (Jun and Im, 2000). Alternatively, Li and Liu (2000) use the total plastic strain tensor e^p as the threshold field when performing refinement for mesh-free methods. In the quasicontinuum literature, strain is also used to gauge whether a continuum simulation is reliable enough in a particular region (Miller and Tadmor, 2002). While e^p offers a good starting point, its cumulative nature renders it insufficient to detect shear bands in an arbitrary granular flow system; large strain often appears everywhere eventually, even without the presence of shear bands, e.g., in a column collapse. We thus opt for plastic strain $rate \dot{e}^p$, taking advantage of the instantaneous nature of this field.

Another way to think about where we want to replace the continuum with discrete grains is to decide where we trust the continuum model the least. Since the continuum model adopted here is local in nature (i.e., the pointwise stress is a function of the

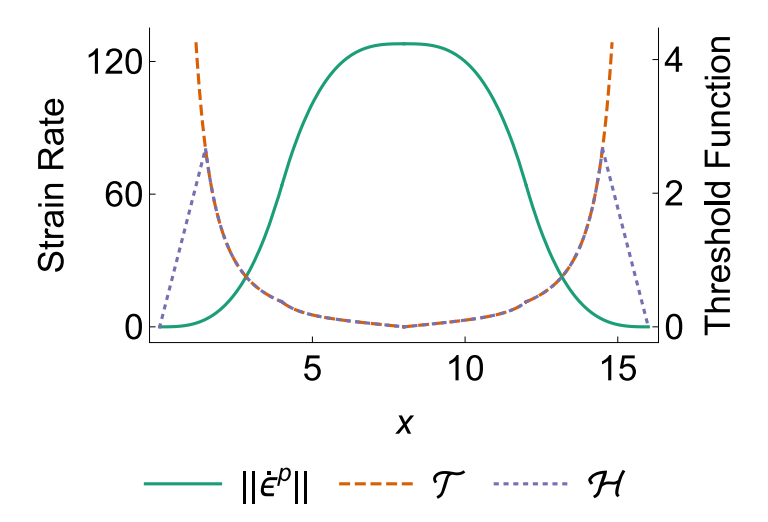


Fig. 3. One-dimensional example of the hybrid oracle constructed through cubic splines. A localized plastic strain rate field is plotted as the green, solid curve. The thresholding function \mathcal{T} corresponding to this strain rate field is plotted as the orange, dashed line. The high value of the thresholding function corresponds with the boundary of the shear band. The purple, dotted line is the regularized oracle \mathcal{H} . Compared to \mathcal{T} , the regularized oracle \mathcal{H} is now bounded.

pointwise strain only), the continuum model loses credibility when the flow varies sharply (i.e., the strain rate has large gradients) compared to the grain size. This is not to say that wherever there is a high strain rate the continuum model is not trustworthy; rather, wherever there are high strain rate *gradients*, the continuum model cannot be trusted. Indeed, by definition, the shear localization problem experiences a high strain rate gradient on the boundary of the shear band. Thus, when designing an oracle to locate the shear band, it is crucial that we precisely measure the sharp flow features.

3.1. Detecting shear bands using the strain rate Laplacian

With that in mind, the Laplacian of the plastic strain rate $\nabla^2 \dot{e}^p$ gives us a good estimate of the boundary of shear bands. To ensure a rate independent oracle that captures both rapidly and slowly flowing shear bands and to introduce a grain characteristic length scale, we propose the following nonlocal thresholding function,

$$\mathcal{T}(\mathbf{x}) = \left| \frac{\nabla^2 \|\dot{\mathbf{c}}^p\|}{\|\dot{\mathbf{c}}^p\|} \right| > \frac{c_0}{D_{50}^2},$$

where the mean diameter of the discrete grains D_{50} introduces a grain-size dependence and c_0 is a dimensionless user input parameter. When $\mathcal{T}(x)$ is larger than $\frac{c_0}{D_{50}^2}$, we consider x to be on the boundary of the shear band.

To better explain the concept, we provide a didactic example. As shown in Fig. 3, consider a one-dimensional, localized plastic

To better explain the concept, we provide a didactic example. As shown in Fig. 3, consider a one-dimensional, localized plastic strain rate field (constructed through cubic splines and plotted as the green, solid curve); its corresponding $\mathcal{T}(x)$ field is displayed as the orange, dashed line. Notice how the high value of $\mathcal{T}(x)$ is observed on the boundary of the original localized flow field. Fig. 6b shows the shear band boundary identified by the oracle in an actual continuum simulation. Note that even though Fig. 6b displays a horizontal and straight shear band boundary, it is neither necessarily horizontal nor straight in general.

To keep \mathcal{T} well defined physically and numerically when $\|\dot{\epsilon}^p\|$ is vanishing, we substitute a regularized plastic strain rate $\|\dot{\epsilon}^p\|_{max}$ in the denominator, obtaining:

$$\mathcal{H}(\mathbf{x}) = \begin{cases} \left| \frac{\nabla^2 \| \dot{\mathbf{e}}^p \|}{\| \dot{\mathbf{e}}^p \|_{max}} \right| & \| \dot{\mathbf{e}}^p \|_{max} > 0 \\ 0 & \| \dot{\mathbf{e}}^p \|_{max} = 0 \end{cases},$$

where

$$\|\dot{\boldsymbol{\epsilon}}^p(\boldsymbol{x})\|_{\max} = \max_{\boldsymbol{y} \in N_r(\boldsymbol{x})} (\|\dot{\boldsymbol{\epsilon}}^p(\boldsymbol{y})\|)$$

and $N_r(x)$ is the neighborhood of x, consisting of all y such that ||y - x|| < r for some r > 0. In practice, we process \mathcal{H} on the MPM grid node and use the incident cells as the neighborhood. The regularized version of the didactic example is displayed in Fig. 3 as the purple, dotted curve, which is bounded from above.

3.1.1. Mesh dependent threshold

In order to obtain a mesh *independent* solution, it is important to have a mesh *dependent* oracle that eliminates the effect of mesh resolution. In addition to D_{50} , the MPM background grid resolution ΔX is also included in the thresholding process. If $\mathcal{H}(x)$

is larger than either $\frac{c_0}{D_{50}^2}$ or $\frac{c_0}{\Delta X^2}$, we consider x to be part of the shear band boundary. The mesh resolution may thus affect which threshold is first reached. If mesh resolution is low, $\mathcal{H}(x)$ would reach $\frac{c_0}{\Delta X^2}$ first. On the contrary, if mesh resolution is high, $\mathcal{H}(x)$ would reach $\frac{c_0}{D_{50}^2}$ first. Intuitively, if the mesh resolution is low, sharp flow features would be lost artificially. Therefore, the oracle has to be triggered with a lower threshold. Appendix D offers a detailed illustration of the mesh-independent thresholding result.

3.2. Filtering out transient shear bands using recent strain

While the regularized oracle \mathcal{H} provides us with a robust framework to work with, it would also locate both *persistent* and short-lived *transient* shear bands. However, an ideal oracle would only identify the persistent shear bands and not the transient ones. Therefore, we introduce further temporal filtering of the oracle by using the plastic strain Δe^p accumulated in the recent τ_l period of time, $\Delta^{\tau_l} e^p$. Persistent shear bands have significantly larger accumulated plastic strains compared with transient shear bands. Note that we only consider the strain accumulated recently to avoid falsely identifying regions that were shearing in the past but are no longer shearing. This also provides consistent results if the simulation starts at a different point in time. Concretely, the temporally filtered version of the regularized Laplacian based oracle is

$$\mathcal{H}(\mathbf{x}) = \begin{cases} \left| \frac{\nabla^2 \|\dot{\epsilon}^p\|}{\|\dot{\epsilon}^p\|_{max}} \right| & \|\dot{\epsilon}^p\|_{max} > 0 \quad \text{and} \quad \|\Delta^{\tau_l} \epsilon^p\| > c_1 \\ 0 & \|\dot{\epsilon}^p\|_{max} = 0 \quad \text{or} \quad \|\Delta^{\tau_l} \epsilon^p\| <= c_1 \end{cases},$$

where c_1 is another dimensionless user input that decides how much plastic strain a point must undergo in order to be considered a candidate for the shear band oracle. In practice, we choose c_1 to be no more than 5%. To avoid rate-dependence, we choose τ_l to be inversely proportional to the maximum shear rate of the entire system at each time step, i.e., $\tau_l = \frac{c_l}{\hat{\gamma}_{max}}$, where $\hat{\gamma}_{max}$ is the maximum shear rate, while c_l is a dimensionless constant. To further filter out transient events, when applying the oracle, we maintain a global constraint that the set of all the hot spots identified by the oracle must remain unchanged (no addition or removal of hot spot) for a certain period of time τ_g before we consider these hot spots a legitimate shear band ready to be enriched with discrete grains. Choosing τ_g too small will result in false identification of transient shear bands. A value too large will result in a delay of shear band identification; the simulation would experience the mesh dependence inaccuracy of the continuum simulation. Similar to τ_l , we also pick τ_g to be inversely proportional to the maximum shear rate to avoid rate-dependent results, i.e., $\tau_g = \frac{c_g}{\hat{\gamma}_{gax}}$, where c_g is a dimensionless constant. We emphasize that these are not fundamental timescales of shear banding granular flows but rather heuristics that guarantee the rate-independence of the hybrid oracle, which will now detect fast-and-slow flowing shear bands alike, enriching the faster flow earlier and the slower flow later (Appendix E).

Putting everything together, we have the complete shear band detection scheme listed in Algorithm 1. The exact oracle coefficients are listed alongside the experiments in Tables 4, 6, and 9.

Algorithm 1 Shear_Band_Detection

```
1: flagged_region \leftarrow \emptyset
2: for x \in \text{Continuum\_Background\_Grid\_Nodes} do
3: if \|\dot{\epsilon}^p(x)\|_{max} > 0 and \|\Delta^{r_l} \epsilon^p(x)\| > c_1 and \left|\frac{\nabla^2 \|\dot{\epsilon}^p\|}{\|\dot{\epsilon}^p\|_{max}}\right| > \min\left(\frac{c_0}{D_{50}^2}, \frac{c_0}{\Delta X^2}\right) then
4: flagged_region.insert(x)
5: end if
6: end for
7: if flagged_region! = \emptyset and \Delta^{r_g} flagged_region = \emptyset then
8: return True
9: else
10: return False
11: end if
\Delta^{r_e} is the difference accumulated over the past time \tau_*
```

3.3. Oracle comparison

While simpler oracles may at first seem appealing for shear band detection, we show that our carefully-chosen oracle is applicable in a wider range of scenarios. We test different oracles' ability to identify shear bands on three classical, characteristic cases. The first case is planar shearing of an over-consolidated specimen where a shear band nucleates from weak elements. The second case is planar shearing of an under-consolidated specimen, in which case the entire specimen flows and shear does not localize. The third case is a triaxial test where a shear band forms in the middle of the domain diagonally. An oracle that is *discerning* – that is, possessing sensitivity and specificity in determining shear bands – should flag regions of the shear band and *only* regions of the shear band in the first and the third cases while reporting no shear band in the second case. In other words, a discerning oracle should not display false positive or false negative results.

In Fig. 4 we show oracles using the strain rate threshold (Jun and Im, 2000) and the total strain threshold (Li and Liu, 2000) as the shear band criteria. Yellow regions are flagged by the oracle as parts of the shear band. Both criteria correctly detect the

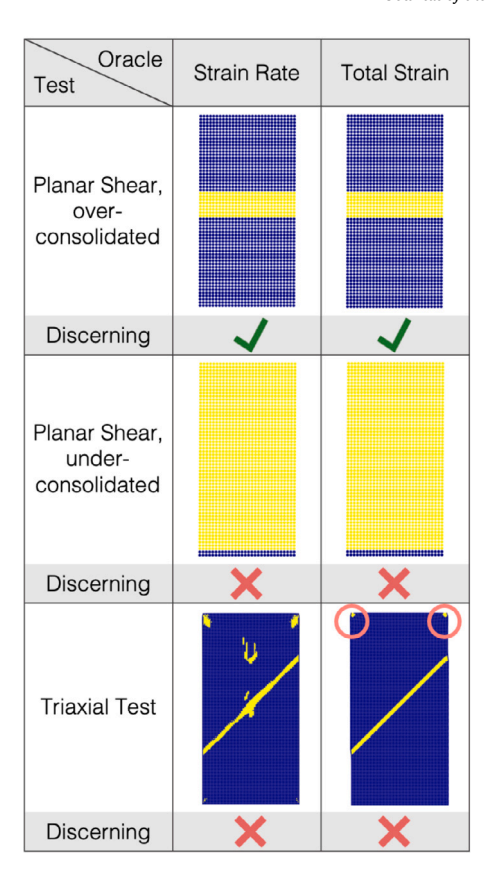


Fig. 4. Failed oracles: strain rate and total strain. Both criteria result in non-discerning shear band detection in the under-consolidated planar shear case and the triaxial test.

shear band in the over-consolidated planar shear case. However, both criteria falsely flag shear banding in the under-consolidated case, and for that matter, would flag banding in any geometry that produces a steady flow without localization (e.g., flow down an inclined chute). It can be argued that the strain rate criterion can be tuned higher to avoid such a false-positive result. However, in that case, a faster flow rate would still falsely trigger the threshold. Hence, there is an ambiguity in selecting a time-scale to define a strain rate threshold. Furthermore, both criteria fail to be discerning in the triaxial test. The strain rate criterion flags the transient high shearing region that is not part of the persistent shear band. While the total strain is not as affected by transient events, it is highly sensitive to the history. It falsely identifies the corner regions near the top plate. These regions undergo large strain at the beginning of the simulation due to the elastic membrane closing in on the top plate.

We thereby avoid using the strain rate and the total strain as the shear band criteria and consider the regularized strain rate Laplacian (Section 3.1 and Section 3.2). Fig. 5 demonstrates the effectiveness of our oracle. Both the Laplacian and recent strain identify the shear band in the over-consolidated planar shear case. The Laplacian oracle also successfully avoids false identification of the shear band in the under-consolidated case since there is no strain rate gradient. On the contrary, the recent strain, similar to the strain rate and the total strain, incorrectly flags the entire shearing region as shear banding. In the triaxial test, the strain rate Laplacian, like the strain rate criterion, is sensitive to transient high shearing regions and incorrectly flags the region outside of the persistent shear band. By contrast, the recent strain oracle correctly detects the persistent shear band, and unlike the total strain, it is not affected by the entire strain history and does not flag the top corners of the specimen. As shown in the third column, combining the strain rate Laplacian and the recent strain, we have a shear band detection scheme that is discerning in all three scenarios. It is worth noting that while we present a discerning oracle with the goal of robust shear band detection in arbitrary flow cases, simpler oracles with fewer components can be used when only a certain type of shear band behavior is expected.

4. Enrichment with discrete grains

Once the boundary of the shear band is identified by the oracle, we swap the continuum near the shear band boundary with discrete grains. During the swapping process, we maintain an overlapping region of thickness t_h consisting of both discrete grains and continuum MPM particles. As shown in Figs. 6f and 8, this reconciliation/handshaking domain allows us to couple the discrete zone with the continuum zone (Xiao and Belytschko, 2004). In practice, we set t_h to be one MPM cell width. Details of the coupling algorithm are listed in Section 5.

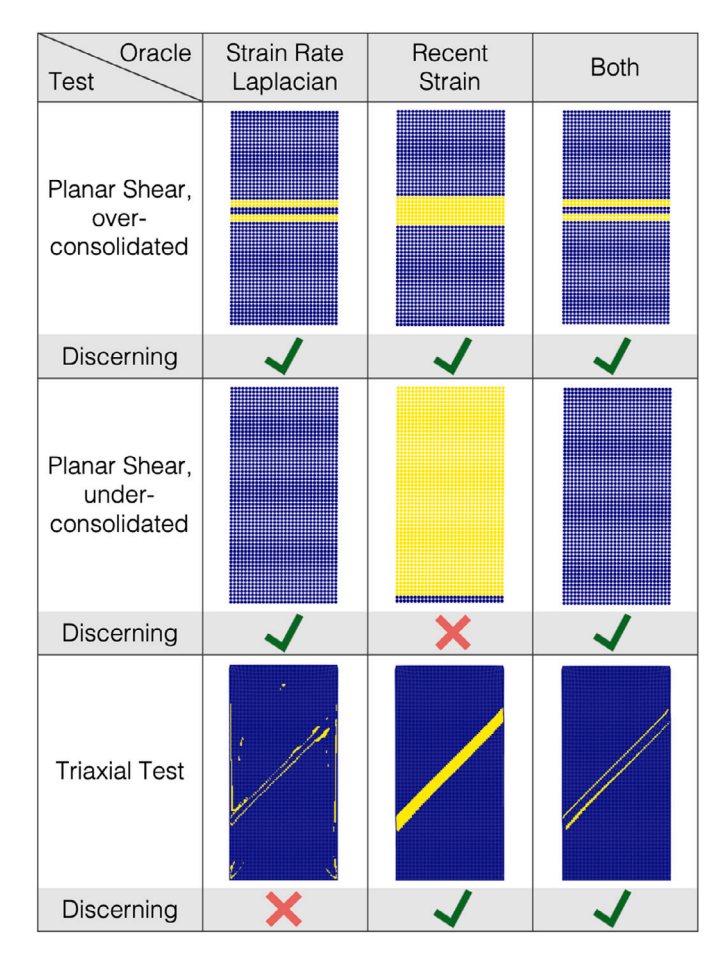


Fig. 5. Our oracle uses both the strain rate Laplacian and the recent strain, and provides discerning shear band detection in all three cases.

The precise steps of the swapping routine are as follows: after we obtain a level set ϕ_b of the boundary of the shear band (Fig. 6b) through thresholding on \mathcal{H} , we define the signed distance $\phi_d(x)$ (Fig. 6c) to this level set. Based on a user defined distance ϕ_0 (Fig. 6d), we label a point x to be inside the discrete grain zone if $\phi_d(x) \le \phi_0 + \frac{1}{2}t_h$ and x to be inside the continuum zone if $\phi_d(x) > \phi_0 - \frac{1}{2}t_h$. For x inside the discrete grain zone but not in the reconciliation zone, all the continuum MPM particles will be replaced with discrete grains (Fig. 6e and f).

Clearly, a key element during the enrichment operation is the choice of ϕ_0 . Choosing ϕ_0 too small leads to a discrete zone thickness too small to cover the whole shear band, whereas choosing ϕ_0 too large leads to excessive numbers of discrete grains, which decreases computational speed. In general, a wide range of shear band thickness t_s (Kuhn, 2017; Finno et al., 1997; Alshibli and Sture, 1999; Desrues and Viggiani, 2004; Guo, 2012) has been observed in experimental studies, from $10D_{50}$ to $30D_{50}$.

For the purpose of hybrid simulation, we set ϕ_0 so that after enrichment the thickness of discrete grain zone t_d is larger than the thickness of the presumed shear band t_s , i.e., the discrete grain zone is at least thick enough to resolve the shear band so that the shear band does not shear into the continuum. In practice, we adopt the heuristic of setting ϕ_0 no more than $30D_{50}$ so that the thickness of the discrete grains region near each boundary is no more than $60D_{50}$. We found that for certain geometries, the shear band is thinner than others, and a smaller ϕ_0 can be used to further reduce the computational cost.

4.1. Packing for enrichment: from macro to micro

Now that we have decided where to put the discrete grains, what remains to be answered are the exact properties of the discrete grains. We wish to replace the continuum in the shear band with discrete grains of the same total mass and momentum (Yue et al., 2018). However, the same stress, strain, and history are also desirable. This reflects a well-known challenge in granular media modeling: how to find a microscopic discrete packing with identical properties to a macroscopic continuum granular model (Jaeger, 2015). Our goal should be contrasted against the easier task of homogenizing a discrete packing to a continuum state. Our goal requires embedding the lower-dimensional continuum configuration space into the higher-dimensional discrete configuration space; such an embedding problem is inherently under-determined. By contrast, projecting (or "coarse-graining")

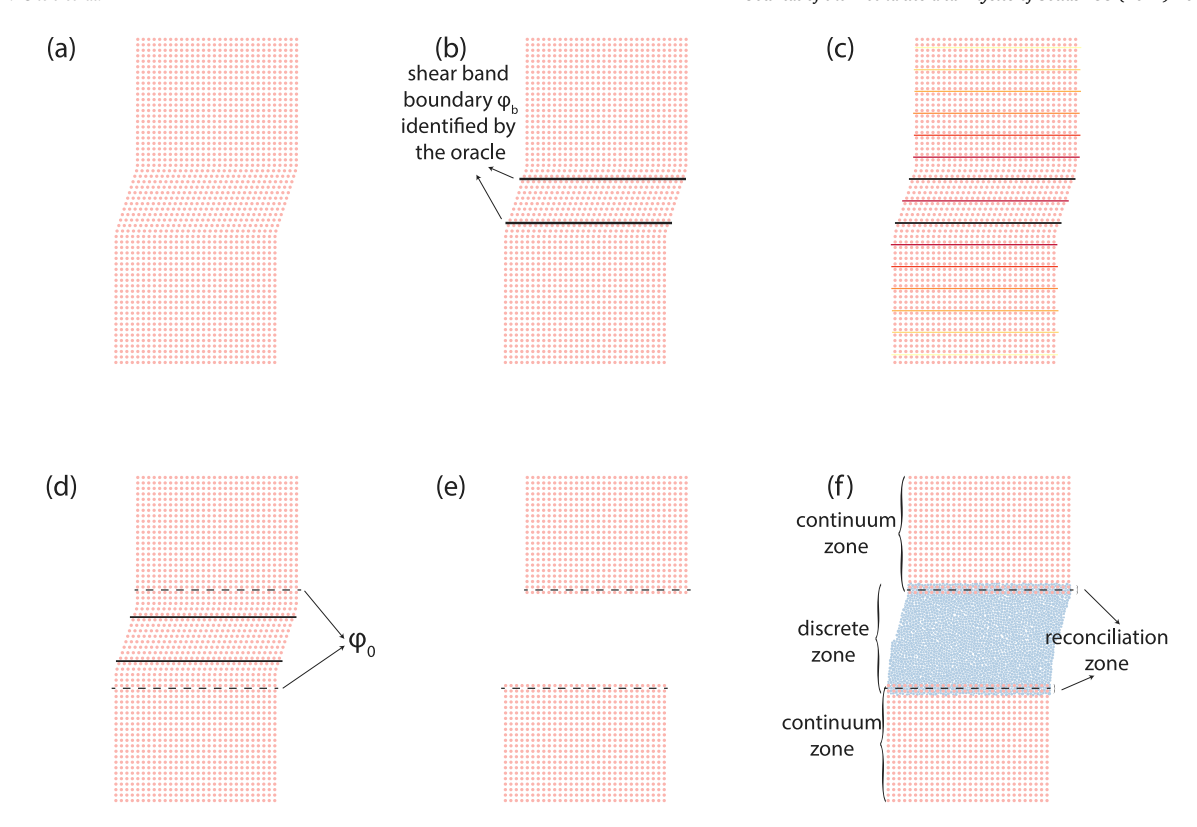


Fig. 6. Illustration of the hybrid oracle (Section 3) and enrichment (Section 4): (a) A continuum shear band forms in a purely continuum MPM simulation. (b) Thresholding on the oracle \mathcal{X} identifies the shear band boundary level set ϕ_b . (c) Across the domain, we compute the signed distance to the shear band boundary level set, indicated by lines in lighter shades of red as the distance increases. (d) We select a user-defined distance ϕ_0 (Section 4) that serves as the boundary of the discrete enrichment zone. We denote this critical distance as a solid black line. Note that in this illustration, the nearest distance to the boundary of every point between the two shear band boundaries is smaller than ϕ_0 . Depending on the choice of ϕ_0 , this may not be the case in general. (e) We delete all continuum MPM points that fall within the region defined by this critical distance. (f) After deletion, we fill the region with discrete grains that ensure compatibility between the replaced continuum and the newly added discrete grains. The tools for enforcing compatibility are detailed in Section 4.1. An overlapping region between the continuum zone and the discrete zone is maintained in order to couple the two zones (Section 5).

the higher-dimensional discrete state onto the lower-dimensional continuum-state is straightforward via strain computation (Bagi, 2006) and stress averaging (Christoffersen et al., 1981).

One can adopt a random sampling technique to generate a packing with desired properties (O'Hern et al., 2002), i.e., algorithmically compute a discrete packing with target packing fraction, stress, etc. This method is adopted by Yue et al. (2018) and Chantharayukhonthorn (2019). However, the packings produced by this method did not reach the density required for shear banding problems. The two-point-tangent scheme of Chantharayukhonthorn (2019) generates packing with a packing fraction as high as 84%. Yet not even that is high enough for shear banding simulation of 2D disks. In the context of shear band modeling, a high packing fraction is necessary for initiating the shear band since the material has to be able to dilate in order to experience softening in a particular region where the shear band will form. The discrete packing we use can exhibit a packing fraction as high as 86%. In addition to the challenge of achieving a high packing fraction, there is no obvious way to match continuum stress and history-dependent state variables with the random sampling technique. Therefore, instead of adopting a random sampling technique for packing generation, we directly sample discrete grains from a single, naturally simulated discrete packing, e.g., by pouring discrete grains into a container under gravity. This packing is also used as the initial packing for the fully discrete shear band simulation that serves as the ground truth for the hybrid simulation. To obtain a high packing fraction, we adopt the approach of Cundall (1989) and prepare the packing under low friction value ($\mu = 0.01$); μ is then set to the usual value of 0.5 for the subsequent simulations. Using such a packing satisfies the requirement of a high packing fraction, but it remains a task to match the continuum stress and the history-dependent state variables when enrichment is invoked.

4.1.1. Sample preparation through kinematic training

Theoretically, given a packing of discrete grains, to solve the macro to micro problem, we can optimize the position of each grain such that certain stress and state variable constraints are satisfied. However, this is a difficult problem in general, due to the global coupling among grains and the combinatorial nature of discrete grains. We thereby do not intend to solve a general optimization problem but propose a heuristic approach of *preparing* the discrete packing so that it best matches the continuum to be replaced.

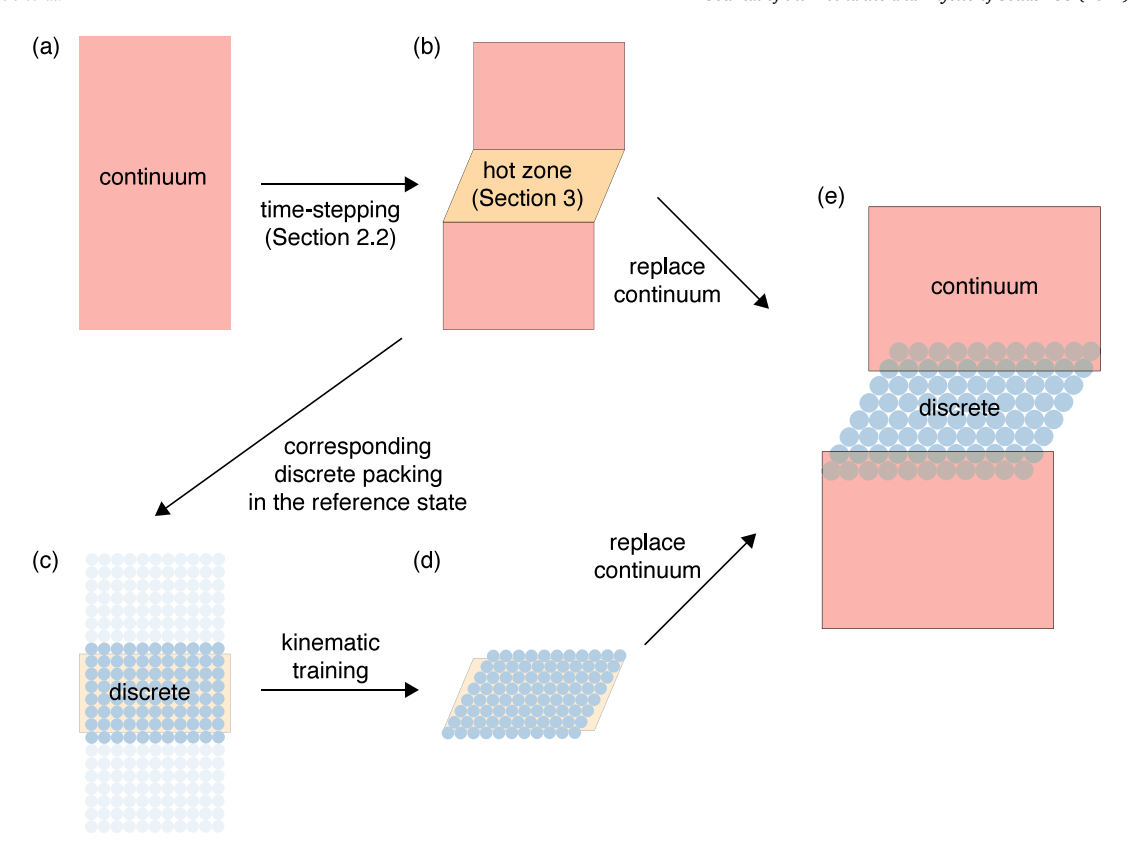


Fig. 7. Illustration of kinematic training. (a) The simulation is initialized with continuum throughout the whole domain. (b) After continuum time-stepping (Section 2.2), a shear band forms in the middle of the domain (the yellow hot zone) and is identified by the hybrid oracle from Section 3. (c) We then identify the corresponding discrete packing in the reference state. (d) This discrete packing is kinematically trained by enforcing the continuum motion as a boundary condition. (e) After training, the newly trained packing replaces the continuum shear band in the original simulation. From now on, the hybrid simulation continues with the discrete grains simulating the shear band.

The intuition behind "kinematic training" is that if the discrete grains underwent the same history of deformation as the continuum, they would also have similar stresses and state variables, such as fabric tensor and void ratio.

As shown in Fig. 7, at the time of enrichment, the continuum region in the middle of the domain has undergone significant shearing. The hybrid oracle (Section 3) identifies this shearing region (Fig. 7b). To replace this continuum shear band, the kinematic training scheme first obtains the discrete packing (Fig. 7c) corresponding to the reference state of the continuum shear band. Such a packing can be grabbed from a fully discrete version of the initial system. The kinematic training scheme then starts a separate, temporary discrete simulation of this discrete packing. This separate simulation only simulates the portion in the shear band region. This simulation is kinematically constrained such that at the end of this temporary simulation the discrete packing (Fig. 7d) has the same boundary deformation as the continuum domain it is replacing. In practice, the deformation is enforced by kinematically prescribing a moving boundary of the discrete packing. The original simulation is paused in time throughout the training process. After kinematic training is completed, the kinematically trained packing is used to replace the continuum shear band in the original simulation (Fig. 7e). After this, the original simulation unfreezes and continues time-stepping now as a hybrid simulation.

The kinematic stress and state variable training possesses several key features. First, it can be applied in scenarios with arbitrary boundary conditions without ad-hoc modifications. All it requires is applying the deformation of the continuum onto the discrete. Second, the kinematically trained packing will fit the hybrid enriched zone perfectly since at the end of the training process, the discrete packing underwent exactly the same boundary deformation as its continuum counterpart. This is a significant advantage over a non-kinematic based training scheme that concentrates on optimizing stress and internal state variables without properly constraining the kinematics. Third, kinematic training is computationally economical since we simulate only a small portion of the original discrete packing.

Kinematic training also has limitations. Its performance depends on the accuracy of the continuum simulation in terms of its ability to deform the same way as a fully discrete simulation. Training with a poorly calibrated continuum model leads to imprecise stress in the discrete packing. Furthermore, in the case of a small domain, due to the Hill-Mandel homogenization condition (Hill, 1963; Mandel and Dantu, 1963), when the same strain is applied to a finite discrete packing and a corresponding continuum model respectively, the discrete packing exhibits a larger stress than the continuum. Additionally, since we enforce the deformation on

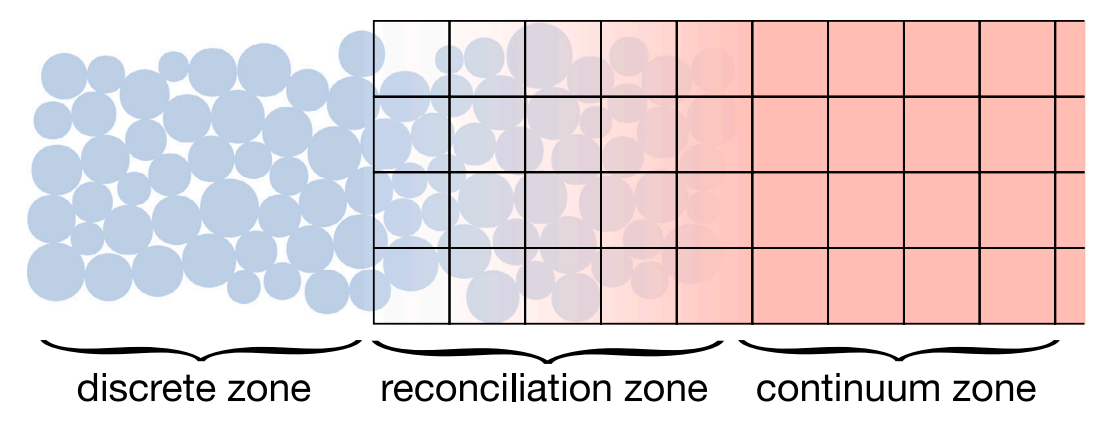


Fig. 8. After enrichment, the discrete zone and continuum zone are time-stepped together (Yue et al., 2018). Inside the reconciliation zone where both discrete grains and continuum MPM particles exist, the per-element average velocities of both systems are constrained to be identical.

the boundary, there is no guarantee that the element-level deformation is matched between the trained discrete packing and the continuum simulation.

A similar kinematic technique is also reported in the hierarchical multiscale literature, where continuum strain is applied to a discrete packing (Fish, 2013). However, their goal differs from ours as they do not intend to prepare a discrete packing with the same characteristics as a simulated continuum packing, but rather to generate a constitutive response from a discrete packing. Cases there are also usually limited to a periodic Representative Volume Element (RVE). By contrast, the kinematic training we propose here assumes no periodicity and applies to packings of arbitrary shape and size.

Learning from early attempts. We first attempted to kinematically train the discrete packing by enforcing continuum motion onto every single grain of the discrete packing. However, doing so overly constrains the motion of individual grains, which prevents the discrete packing from building the correct stress. For example, in a continuum simple shear simulation, the velocity is completely linear. However, in a discrete simple shear simulation, the motion of each individual grain is highly nonlinear with violent rotation and packing reconfiguration, though their homogenized velocities are linear. Therefore, if we enforce the continuum motion onto each individual grain, the discrete simulation would yield an incorrect shear stress. We thereby opt to enforce continuum motion not at the *individual* grain level but at the *entire* packing level. In essence, this translates to enforcing continuum motion only on the boundary of the discrete packing.

5. Hybrid discrete-continuum coupling

In this section, we will discuss how to couple the continuum zone and the discrete zone together so they form a coherent simulation as a whole. During a hybrid simulation, (1) and (2) continue to describe the dynamics in the discrete and continuum zone, respectively. However, additional treatment is needed in the hybrid reconciliation zone where discrete grains and continuum MPM particles coexist (Fig. 8). Inside the reconciliation zone, we follow the approach of Yue et al. (2018), where continuum MPM particles and discrete grains are constrained to have identical velocity in a homogenized sense. We recap the major points of the algorithm and refer to the original paper for details.

The discrete and continuum systems are coupled in the reconciliation zone via

$$\begin{cases} w\rho \frac{Dv^d}{Dt} &= wf^d & +f^{c\to d} \\ & \text{unconstrained step} & \text{constrained step} \\ (1-w)\rho \frac{Dv^c}{Dt} &= (1-w)f^c & -f^{c\to d} \\ & \text{unconstrained step} & \text{constrained step} \end{cases},$$

$$v^d &= v^c$$

$$(9)$$

where v^d is the homogenized velocity of the discrete system; v^d is computed by interpolating discrete grain velocities onto the continuum background grid using MPM-style Lagrangian-to-Eulerian interpolation (Sulsky et al., 1995); v^c is the grid velocity of the continuum MPM system; f^d is the homogenized version of the force experienced by the discrete system as defined by (1) and f^c is the force experienced by the continuum system on its own obtained from (2); $f^{c \to d}$ is the interaction force exerted from the continuum system to the discrete one subject to the velocity constraint in the reconciliation zone; w is a space time dependent weight function $w(x,t) \in [0,1]$ that partitions the original density into a discrete density and a continuum density, similar to the volume fraction of the mixture theory (Anderson and Jackson, 1967). In practice, we set the partition weight to be a constant of 0.5.

We integrate (9) in an operator-splitting fashion. For the first, unconstrained terms, the discrete and continuum systems are time-stepped independently. Then a constrained/correction step is applied on both systems by computing $f^{c\rightarrow d}$. After applying the

Table 3
Planar shear test specimen information.

Specimen information	Value	Unit
Width	6	cm
Height	12	cm
Number of grains (in discrete-only setting)	7640	
Confining pressure	400	kPa

Table 4Hybrid oracle and enrichment parameters for the planar shear test.

Parameter	Value	Unit
c_0	1.0×10 ⁻⁶	
c_1	1.0×10^{-4}	
c_l	8.0×10^{-4}	
c_g	1.2×10 ⁻³	
ϕ_0	2.2	cm

interaction force on both systems, their velocities become identical. This constrained step is readily enforced on the MPM background grid. In contrast to common solid-fluid coupling algorithms, no linear system is involved, and the algorithm can be easily parallelized. Thus coupling introduces minimal overhead.

This velocity-based kinematic constraint ensures that the two systems' strain rates match, and thereby strains also match over time. While it would be ideal to also match stress, we find the kinematic constraint sufficient to achieve accuracy in our problem scenarios. We believe that this is because, inside the reconciliation zone, the two systems' load responses are sufficiently similar given that the continuum model was calibrated from the discrete. We leave it to future work to explore scenarios where the constitutive laws differ greatly.

Summary of the proposed framework. Putting everything together, we initiate the simulation in a pure continuum fashion. As the simulation evolves (Section 2.2), we constantly check if a continuum shear band has formed, using the hybrid oracle (Section 3). If a persistent shear band has formed, we enrich the simulation by substituting discrete grains in the shear band region (Section 4). We time-step the simulation using the hybrid discrete-continuum algorithm (Section 5). The pseudocode of the complete algorithm is presented in Algorithm 2.

Algorithm 2 Hybrid_Shear_Band_Simulation

```
1: time step \leftarrow 0
2: enriched \leftarrow false
3: while time_step < num_steps do
4:
       if not enriched then
5:
          Continuum time-stepping
                                                                                                                           Section 2.2
6:
          if Shear Band Detection then
                                                                                                           ⊳ Section 3 and Algorithm 1
7:
              Discrete Enrichment
                                                                                                                             ⊳ Section 4
8:
              enriched ← true
          end if
9:
10:
                                                                                                                             ⊳ Section 5
11:
          Hybrid Discrete-Continuum time-stepping
12:
       end if
       time\_step \leftarrow time\_step + 1
13:
14: end while
```

6. Numerical examples

In this section, we demonstrate the robustness of the hybrid algorithm in three different geometries. For each, a discrete simulation made of only discrete grains is treated as the ground truth, and the hybrid algorithm is compared against it in terms of accuracy and efficiency.

6.1. Planar shear

We start with a planar shear test by taking a similar approach as Sun et al. (2013) and Liu et al. (2016). The detailed specimen information is listed in Table 3. The specimen is fixed at its bottom and is sheared horizontally at its top boundary at a constant speed of 2 cm/s. Periodic boundary conditions are applied on the left and right boundaries. A periodic boundary is necessary for a persistent shear band to form in the horizontal direction. In addition, in order for the shear band to form, a constant vertical confining stress of 400 kPa is maintained on the top boundary.

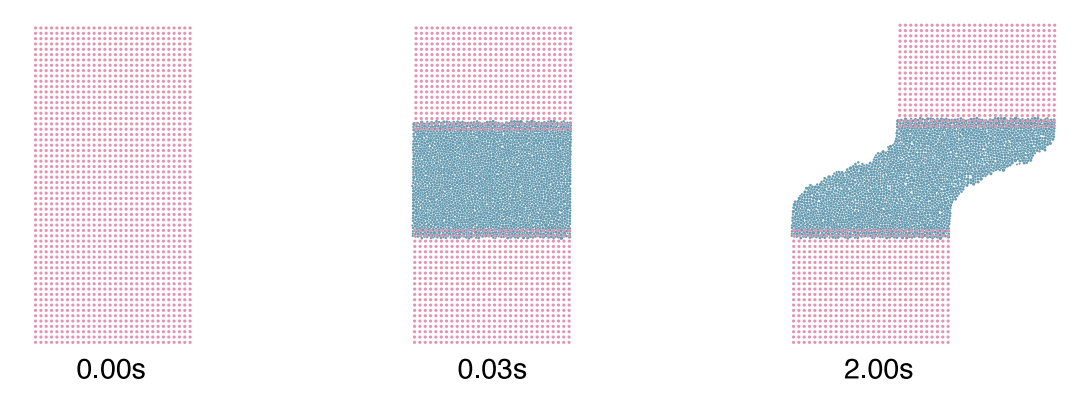


Fig. 9. Hybrid planar shear: beginning of the simulation with only continuum MPM particles (left), immediately after enrichment of discrete grains (middle), and the end of the planar shear test (right).

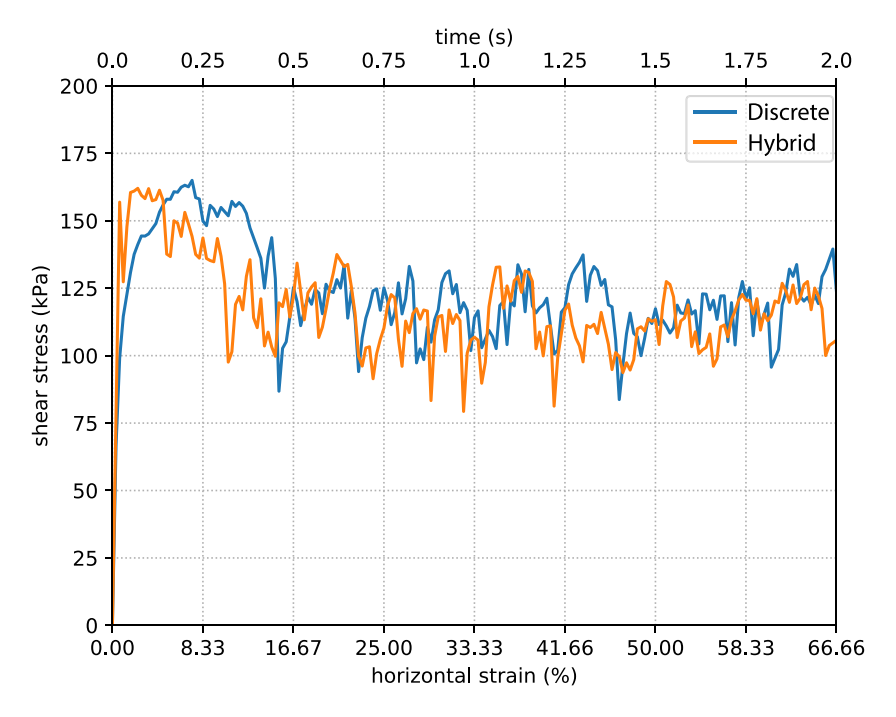


Fig. 10. Shear stress-strain response of the hybrid planar shear simulation, in comparison with a discrete simulation where the entire domain is simulated by discrete grains. An agreement is observed. The shear stress is the tangential force experienced by the top wall divided by the size of the wall. The horizontal strain is the displacement of the top wall divided by the width of the specimen.

Fig. 9 demonstrates the result of the hybrid approach on a planar shear test: the simulation starts with continuum-only MPM particles. Once a continuum shear band is detected by the oracle, the hybrid simulation is enriched with discrete grains. Then the hybrid simulation continues developing a shear band, now captured more accurately by discrete grains. Note that weak continuum MPM particles (that have lower initial packing fractions) have been placed in the middle of the initial continuum specimen in order to break the homogeneity of the specimen and initiate the formation of shear banding. No such practice is required for the discrete simulation, where grain packing variation causes natural inhomogeneity. Note that the location of these weak elements is never passed into the shear band detection oracle.

Fig. 10 demonstrates the macroscopic response of the hybrid planar shear test, where the shear stress is plotted against the horizontal strain. An agreement is observed between the hybrid simulation and the discrete simulation. Both exhibit characteristic strain softening during the formation of shear localization.

Next, we measure the shear band thickness suggested by the hybrid simulation (Fig. 11). Details on how we measure the shear band thickness are listed in Appendix A. Both the discrete and hybrid simulations demonstrate an identical thickness of the horizontal shear band. By contrast, the local continuum simulation on its own suffers from mesh dependence and suggests a shear band thickness of one element size, due to the lack of characteristic length scale in the continuum model.

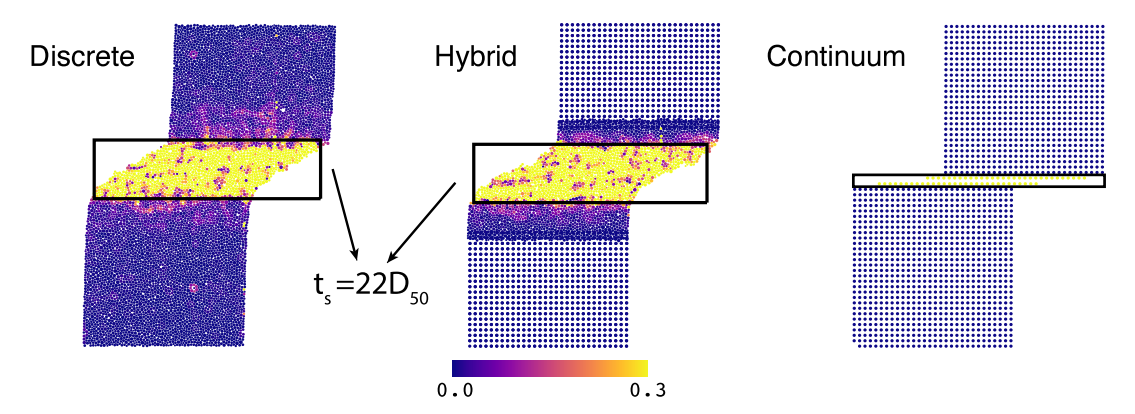


Fig. 11. Planar shear tests simulated by discrete (left), hybrid (middle), continuum (right) methods. Both the continuum MPM particles and the discrete grains are colored by their incremental strains as the specimen's horizontal strain increases from 37% to 57%. The discrete strain is computed through Cundall's best-fit strain (Appendix A). A shear band forms in the middle of every sample; however, the thickness of the shear band differs. Both the discrete and the hybrid approaches present a shear band thickness of $22D_{50}$, while the continuum simulation, due to the lack of characteristic length scale, suggests an erroneous thickness of one element.

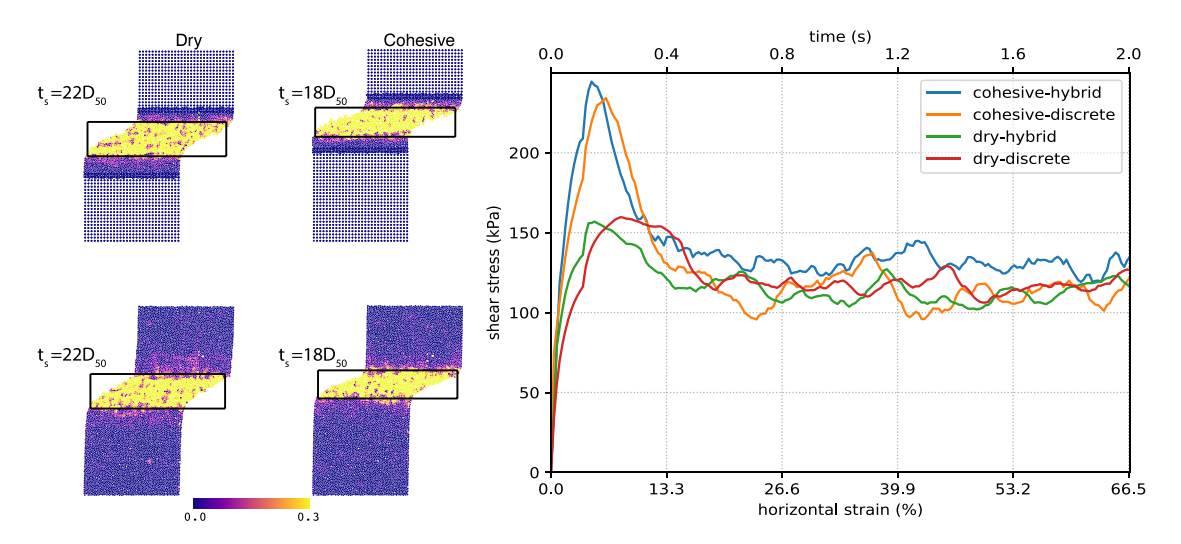


Fig. 12. Planar shear simulations of dry and cohesive granular media. Materials are colored by their incremental strain as the specimen's horizontal strain increases from 37% to 57%. Both the dry and cohesive hybrid shear band simulations predict the same shear band thickness as their discrete counterparts. At the same time, the cohesive shear band is thinner than its dry counterpart. In addition, the cohesive material displays a higher yield stress and more intense softening. Moving average smoothing (with a window size of 8) of the raw data, which acquires 1000 samples per second, has been applied to better illustrate the trend.

6.1.1. Cohesion

To demonstrate the applicability of the hybrid approach to model cohesive granular media, such as soil and powder aggregation, we also run the planar shear test with cohesion activated. Before running the hybrid simulation, we calibrate the continuum cohesion parameter c to the discrete cohesion parameters c_t and c_n so that the same macroscopic yield stress is obtained between the continuum simulation and the discrete simulation.

Fig. 12 compares hybrid simulations of dry and cohesive grains. (The dry simulation is the same as the one in Fig. 11.) Both the dry and cohesive hybrid simulations agree well with their discrete counterparts in terms of the shear band thickness as well as the characteristic softening. Due to cohesion, the cohesive planar shear test produces a thinner shear band, sustains a higher macroscopic yield stress, and experiences more intense softening.

6.1.2. The effect of kinematic training

Here we zoom into the moment of enrichment. Recall that a kinematic training (Section 4.1.1) algorithm has been used to prepare the packing for enrichment so that the inserted discrete packing has a similar deformation history as the continuum. Fig. 13 demonstrates the effect of kinematic training. Without kinematic training, the unloaded packing from the initial discrete configuration possesses a mean shear stress of 6 kPa. After training, the discrete packing holds a mean shear stress of 125 kPa. In

Untrained Trained

150kPa

Fig. 13. Kinematic training of the discrete packing. Shear stress (σ_{xy}) has been plotted. For better comparison, for the ground-truth, full-size discrete planar shear simulation, we color only the corresponding region and leave the rest of the domain in black. The untrained packing is obtained from the initial discrete configuration. The stress of the trained packing is a major improvement from that of the untrained packing and agrees well with the full discrete simulation.

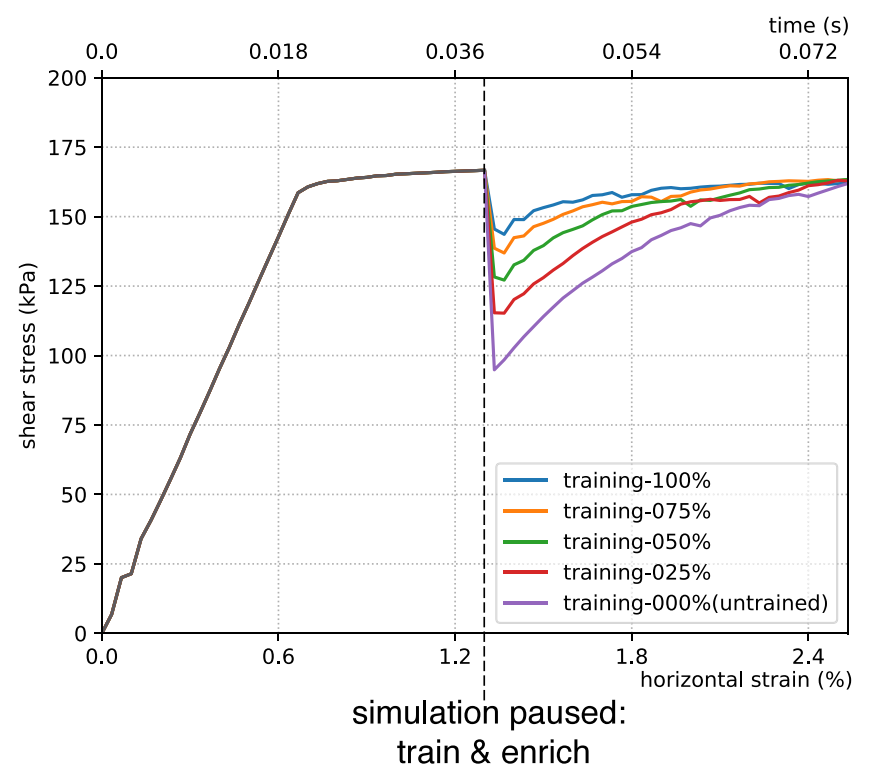


Fig. 14. Hybrid simulation enriched by different discrete packings. The simulation begins fully continuum (gray curve). The hybrid oracle then detects a shear band and pauses the simulation. During this hiatus, kinematic training is applied to prepare a discrete packing, which enriches the continuum shear band. Afterward, the simulation continues. Depending on the amount of training applied, the simulation experiences different levels of stress fluctuation. Untrained packing induces significant unphysical stress fluctuation. The more extensive the training, the milder the resulting stress fluctuation.

Fig. 13 (right), we look at the fully discrete planar shear simulation that has been used as the ground truth (Fig. 11) for the hybrid simulation. The corresponding region in the fully discrete simulation possesses a mean shear stress of 121 kPa. Therefore, the mean shear stress error of the kinematically trained packing is 3%, whereas the untrained packing has an error of 95%. Similar major principal stress directions (from the top left of the domain to the bottom right) are also observed between the trained packing and the packing from the full discrete simulation.

After kinematic training, the packing is used to replace the continuum shear band region in the hybrid simulation. As shown in Fig. 14, we test enrichment with different discrete packings: from no kinematic training, i.e., the packing of Fig. 13 (left), to applying 100% of the continuum deformation at the discrete zone's boundaries, i.e., the packing of Fig. 13 (middle). Without kinematic training, the simulation as a whole suffers from a significant stress fluctuation; with kinematic training, the stress fluctuation is

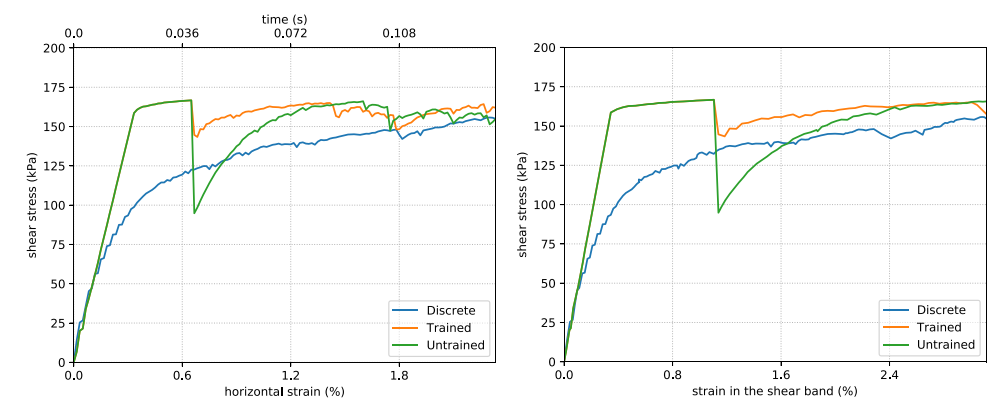


Fig. 15. (Left) Hybrid simulation enriched with kinematically trained packing. Not only does the trained hybrid simulation reduce the serious stress fluctuation caused by the untrained packing, but it also provides a prediction that is now closer to the full discrete simulation. (Right) If we plot the macroscopic stress response with respect to the strain inside the shear band region, we can better observe the hybrid simulation's similarity to the discrete simulation.

Table 5
Triaxial compression test specimen information.

Specimen information	Value	Unit
Width	6	cm
Height	9.42	cm
Number of grains (in discrete-only setting)	5910	
Confining pressure	100	kPa

Table 6

Hybrid oracle and enrichment parameters for the triaxial compression test.

Parameter	Value	Unit
- Turumeter		Oint
c_0	1.0×10 ⁻⁶	
c_1	8.0×10 ⁻³	
c_I	2.0×10 ⁻²	
c_g	9.6×10 ⁻³	
ϕ_0	1	cm

reduced, thereby justifying the effectiveness of kinematic training. We do not expect kinematic training to completely remove stress fluctuation since the continuum deformation cannot be exactly the same as an actual discrete simulation. In fact, a moderate stress drop in comparison with the continuum simulation is desirable in the sense that, as shown in Fig. 15 (left), the hybrid stress is actually now closer to the full discrete simulation. This is due to the fact that the continuum model that initiated the shear band does not model the subloading regime and therefore reaches its peak stress earlier than its discrete counterpart. Therefore, in this early stage of the shear band experiment, the continuum simulation predicts a higher shear stress than the discrete simulation.

Because of this effect, the continuum model also forms a shear band earlier than its discrete counterpart. Thereby, at the same point in time, the continuum simulation possesses a larger strain in the shear band region. To eliminate this mismatch, Fig. 15 (right) re-calibrates the stress response with the shear strain inside the shear band (the size of which is defined by the hybrid oracle) instead of the horizontal strain defined by the movement of the top plate. It can now be better seen that the trained hybrid simulation has an immediate macroscopic shear stress that highly resembles the full discrete simulation.

Another interesting finding is that despite the stress fluctuation, the hybrid simulation rapidly regularizes itself and stabilizes the stress. Even the untrained packing, which has zero shear stress to begin with and suffers from severe stress fluctuation at the point of enrichment, recovers in only 1% of strain. The hybrid simulation is very robust under enrichment disturbance.

6.2. Triaxial compression test

In the triaxial compression test, the periodic boundary condition is replaced by a pressure boundary condition on the lateral boundary. Details on the implementation of the pressure boundary condition are listed in Appendix B.

The details of the specimen used for the triaxial compression test are listed in Table 5. While keeping the confining pressure constant at 100 kPa, this specimen is compressed vertically at a speed of 2 cm per second for 0.5 s where a vertical strain of 10.61% is reached. A no-slip boundary condition is applied to the bottom plane while the material is allowed to slip freely on the top plane. As is the case with the planar shear test, weak continuum MPM particles have been placed in the right lower part of the initial continuum specimen in order to break the symmetry of the specimen.

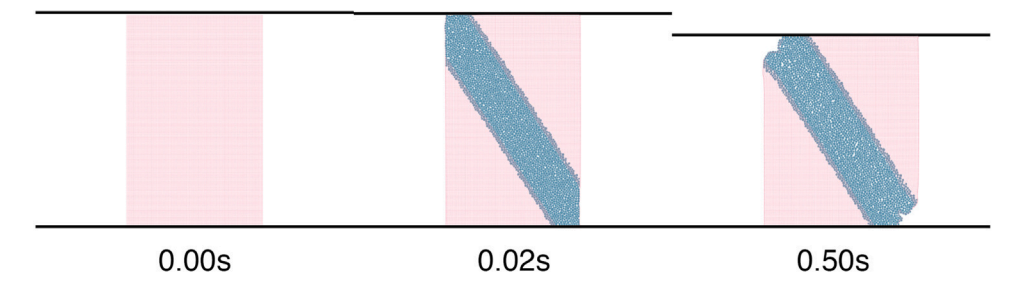


Fig. 16. Hybrid simulation of triaxial compression: beginning of the simulation with only continuum MPM particles (left), immediately after enrichment of discrete grains (middle), and the end of the triaxial test (right).

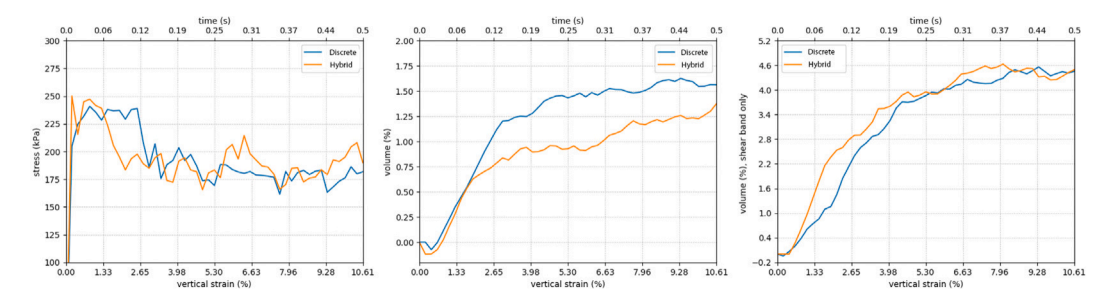


Fig. 17. Macroscopic response of the hybrid triaxial compression test, in comparison with a discrete simulation: stress response (left), volume response (middle), and volume response in the shear band only (right).

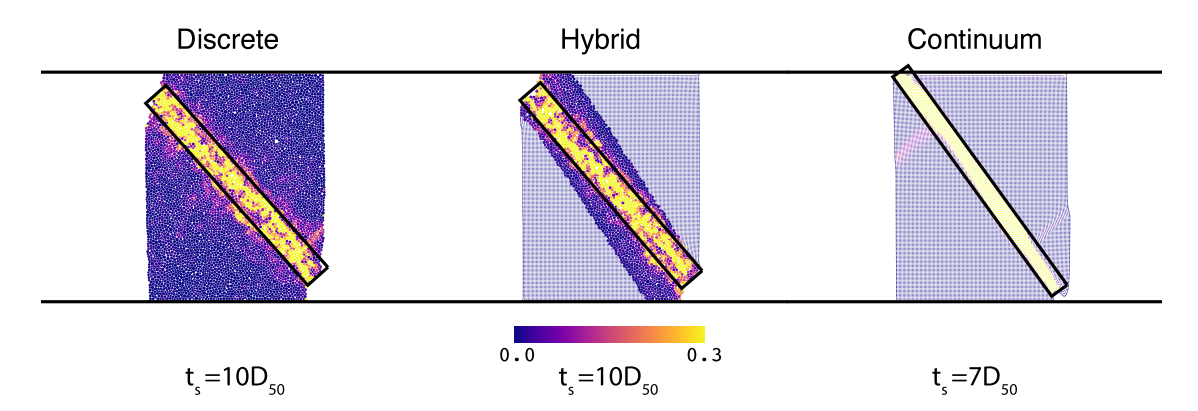


Fig. 18. Comparison of discrete (left), hybrid (middle), and continuum (right) simulation. Both the continuum MPM particles and the discrete grains are colored by their incremental strains as the specimen's axial strain increases from 5.5% to 8.5%. The hybrid simulation suggests a shear band thickness t_s identical to the discrete simulation, while the continuum simulation demonstrates an unphysical $7D_{50}$ shear band thickness.

Fig. 16 demonstrates the hybrid algorithm's ability to simulate shear banding in a triaxial test. In terms of the macroscopic stress response, Fig. 17 (left) exhibits the overall agreement of the hybrid and discrete simulation, albeit an earlier onset of strain softening in the hybrid approach. While Fig. 17 (middle) shows that the overall volumetric strain of the hybrid specimen is smaller than that of the discrete specimen, Fig. 17 (right) demonstrates that the volumetric strain inside the shear band region matches well with the discrete specimen, suggesting that the 0.2% overall volumetric difference comes from the volume expansion outside the shear band. This small difference is therefore a result of our choice of a simple dilation model in the continuum, and one could choose to implement more complex continuum models to lower this error.

As displayed in Fig. 18, the shear band thicknesses t_s for the discrete approach and the hybrid approach match remarkably well: t_s for discrete is $10D_{50}$ and t_s for hybrid is $10D_{50}$ as well. By contrast, the continuum simulation presents an unphysical shear band thickness of $7D_{50}$. For reference, no shear band thickness of less than $10D_{50}$ has been reported in the literature (Kuhn, 2017).

6.2.1. Convergence on enrichment band thickness t_d

In Fig. 19, results from hybrid simulation of increasing discrete enrichment band thickness t_d are shown. Identical shear band thicknesses t_s are obtained by the simulations. In Fig. 20, consistent results are also observed in the macroscopic stress and volume

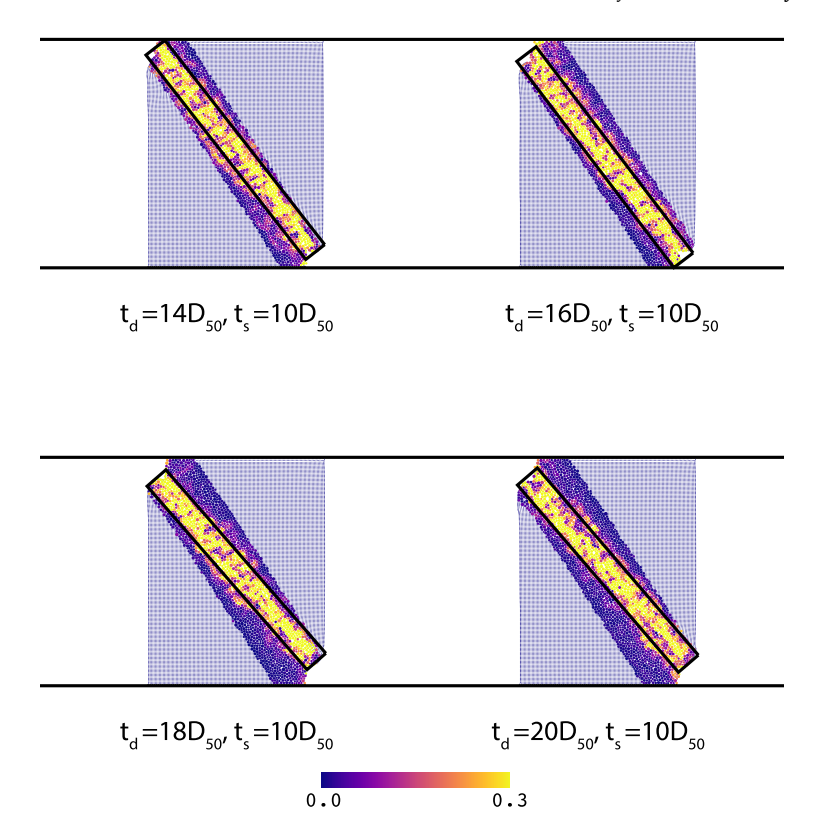


Fig. 19. Hybrid simulation with different discrete enrichment band thicknesses t_d . Identical shear band thicknesses t_s are observed.

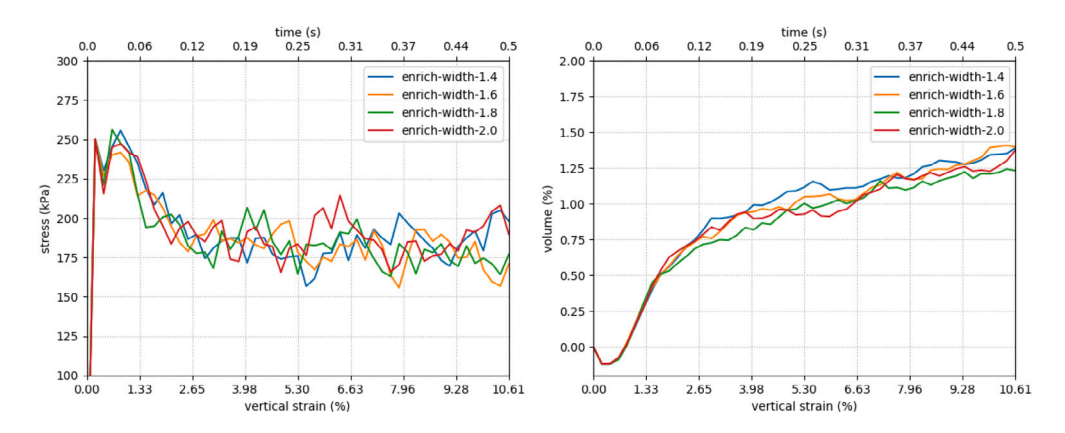


Fig. 20. Macroscopic responses of the hybrid simulation demonstrate consistent results with increasing enrichment band thicknesses t_d .

response. Crucially, as long as the enrichment band thickness is thick enough to capture the shear band, i.e., $t_d > t_s$, the hybrid simulation regularizes itself and provides a converged, grain-size dependent response with no special nonlocal treatment needed.

6.2.2. Mesh independence under refinement

In contrast with the pure continuum simulation that suffers from mesh dependence (Appendix C), the hybrid simulation is mesh independent: similar shear band thicknesses ($10D_{50}$, $11D_{50}$ and $11D_{50}$) are observed in hybrid simulations of high, medium, and low continuum resolutions (Fig. 21).

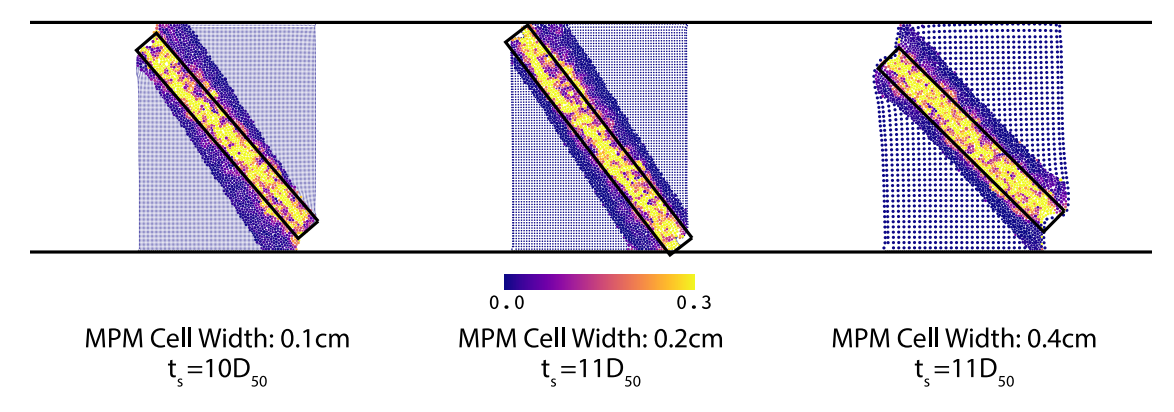


Fig. 21. Hybrid simulations with different MPM resolutions. A similar shear band thickness t, is obtained.

Table 7Plate indentation test specimen information.

Specimen information	Value	Unit
Width	60	cm
Height	20	cm
Number of grains (in discrete-only setting)	125, 176	
Gravity	9.81	m/s^2

Table 8
Plate indentation test intruder information.

Intruder information	Value	Unit
Width	5	cm
Height	2	cm
Velocity	5	cm/s

Table 9
Hybrid oracle and enrichment parameters for the plate indentation test.

$\begin{array}{cccccccccccccccccccccccccccccccccccc$		1	
c_1 8.0×10 ⁻³ c_l 2.0×10 ⁻² c_g 9.6×10 ⁻³	Parameter	Value	Unit
c_l 2.0×10 ⁻² c_g 9.6×10 ⁻³	c_0	1.0×10 ⁻⁶	
c _g 9.6×10 ⁻³	c_1	8.0×10^{-3}	
8	c_I	2.0×10 ⁻²	
ϕ_0 2.5 cm	c_g	9.6×10^{-3}	
	ϕ_0	2.5	cm

6.3. Plate indentation

While the previous examples have focused on flows of granular material under the confining pressure, here we demonstrate an example where bent shear bands form during free surface flows. The penetration of large objects into granular material is a canonical problem in granular modeling (Kang et al., 2018; Agarwal et al., 2020, 2021), which has various applications, including terradynamics (Agarwal et al., 2019a) and crater formation (Goldman and Umbanhowar, 2008). During plate indentation, characteristic, quasi-logarithmic-spiral shear bands emerge (Sokolovskii, 1965).

The details of the plate indentation specimen and intruder are listed in Table 7 and Table 8. The granular specimen initially rests in a rectangular container. Then, a rectangular rigid intruder is kinematically scripted to downwardly intrude the center of the granular bed. Throughout the process, the intruder is kept away from the container's boundary to avoid any boundary effects.

The hybrid simulation begins as a pure continuum, and once the shear band forms, the hybrid simulation enriches the shear band with discrete grains. However, in contrast to previous confined cases, where the shear band is generally straight, we observe a curved logarithmic-spiral shear band. Furthermore, while previous cases have one single shear band per geometry, plate indentation has double-crossing shear bands. As shown in Fig. 22, the level-set based oracle successfully detects and enriches the curved, double shear bands.

It is well known from both analytical analysis and numerical experiments that there are three rigid zones exhibiting little flow during plate indentation. Our oracle naturally capitalizes on this physical feature by keeping a continuum zone in each of the three rigid zones, circled red in Fig. 22 (middle), thereby economizing computational resources.

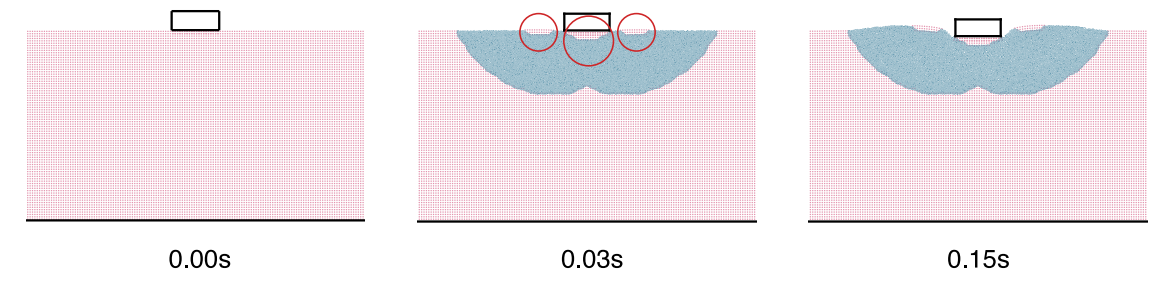


Fig. 22. Hybrid plate indentation: beginning of the simulation with only continuum MPM particles (left), immediately after enrichment of discrete grains (middle), and later in the plate indentation test (right). Notice how the oracle keeps the continuum zone near surfaces at three different spots (under red circles) where there is little or no plastic flow.

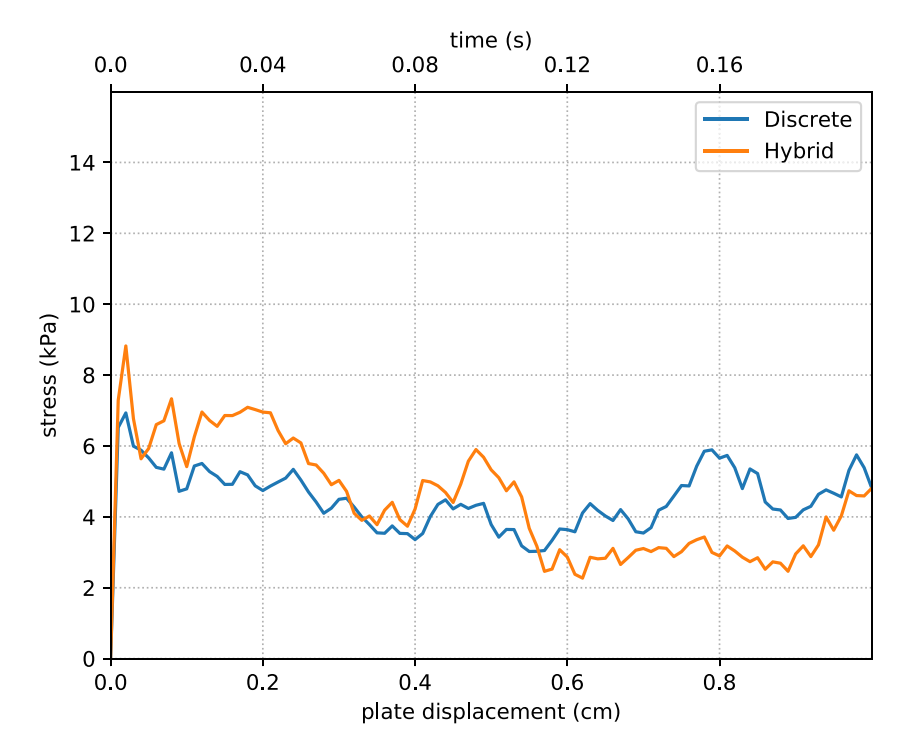


Fig. 23. Macroscopic response of the hybrid plate indentation test, in comparison with a discrete simulation. An agreement is observed. To illustrate the trend, moving average smoothing (with a window size of 8) of the raw data, which acquires 500 samples per second, is displayed here.

Table 10
Total simulation cost (wall time) of the plate indentation test.

Experiment	Type	Cell Width	Minutes	Speedup	Number of Discrete Grains
Plate Indentation	Discrete	n/a	1455	n/a	125,176
Plate indentation	Hybrid	0.5 cm	142	10.2X	14,963

Fig. 23 demonstrates the macroscopic response of the hybrid plate indentation test, where the normal stress on the plate is plotted against its vertical displacement. Hybrid and discrete simulation both exhibit initial softening followed by fluctuation around a constant stress.

Next, we visualize the shear band developed in the hybrid simulation (Fig. 24). Both the discrete and hybrid simulations present similar thickness of the logarithmic-spiral shear band. On the contrary, the local continuum simulation suffers from mesh dependence and produces a thick and blurred shear band, due to the lack of characteristic length scale in the continuum model and a relatively coarse mesh resolution.

We time the hybrid simulation using 16 threads on a desktop computer with a 32-core 2.70 GHz Intel Xeon E5-2680 CPU. We take a time step of $dt = 5 \times 10^{-7}$ s for all of the simulations. As shown in Table 10, the hybrid approach is about 10 times faster than the discrete approach and uses only 14,963 discrete elements.

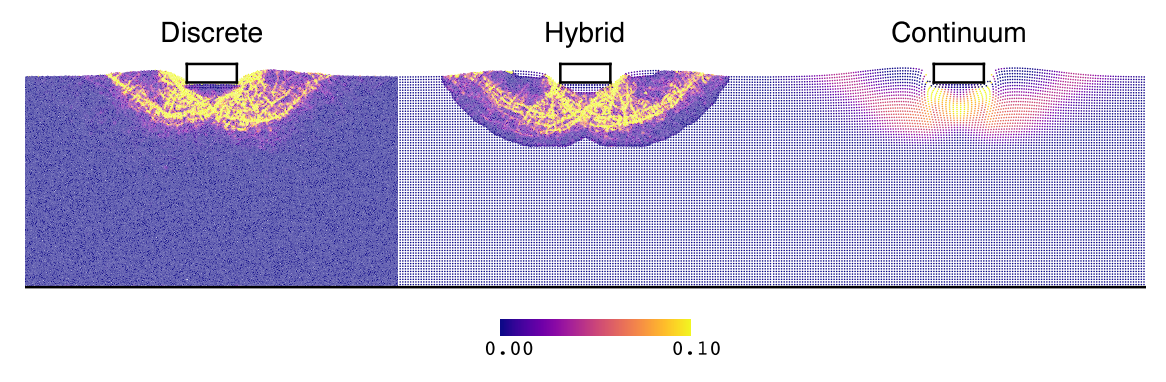


Fig. 24. Plate indentation simulated by the discrete (left), hybrid (middle), and continuum (right) methods. All materials are colored by their plastic shear strains. Although the formation of logarithmic-spiral shear bands in the middle of the sample occurs in all three tests, the thickness of the shear band differs. Both the discrete and the hybrid develop a shear band of similar thickness, while the continuum MPM simulation demonstrates a much thicker shear band due to the incompatibility of the cartesian background grid with the quasi-logarithmic-spiral flow field.

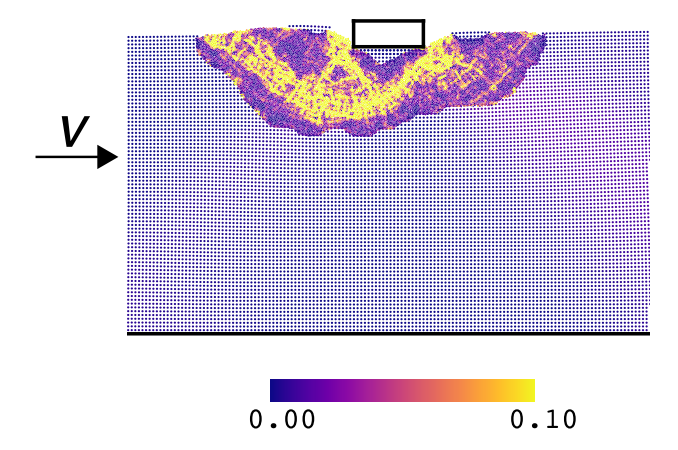


Fig. 25. During the plate indentation test, the left wall is kinematically moved at a constant velocity to represent far-field loading. An asymmetric shear banding structure appears.

6.3.1. Far-field boundary conditions

As a result of using the cheaper continuum approach for handling the outer simulation boundaries, we can capture the effects of far-field boundary conditions efficiently. In Fig. 25, instead of static vertical walls on the left and the right boundaries, we script the left wall to move rightward at a constant velocity of 5 cm/s to represent far-field loading (Zhang and Sagiya, 2018). Such a boundary condition on the continuum region alters the characteristics of the shear bands in the discrete region. Compared to Fig. 24, the left shear band is reinforced and is wider while the right shear band dwindles.

6.4. Large-scale simulations

Now that we have validated the accuracy of the hybrid method in experimental-scale scenarios, we can confidently apply the hybrid approach toward large-scale simulations. Large-scale simulations showcase the efficiency of the hybrid approach because the shear bands are minuscule fractions of the whole simulation domains.

In simulations that involve tens of millions of grains, the computational cost of preparing an aperiodic discrete packing is insurmountable. Therefore, we create periodic discrete-grain packings; these facilitate quick grain insertions into domains of arbitrary sizes. These periodic packings are at least $100D_{50}$ wide to avoid crystallization.

Fig. 26 (left) is a large-scale planar shear test. Like the planar shear test in Section 6.1, we assume periodicity in the horizontal direction. However, the specimen is significantly taller than before, reaching a height of $10,000 \, D_{50}$. The hybrid simulation predicts a localized shear region in the middle of the domain and is 116 times faster than its purely discrete counterpart, which requires nearly a million discrete grains. (Table 11).

Next we set up a large-scale triaxial test. Unlike planar shear, we do not assume horizontal periodicity. Therefore, we have to model the whole domain explicitly. As a result, for the triaxial test in Fig. 26 (middle), which has a height of 12,000 D_{50} and a

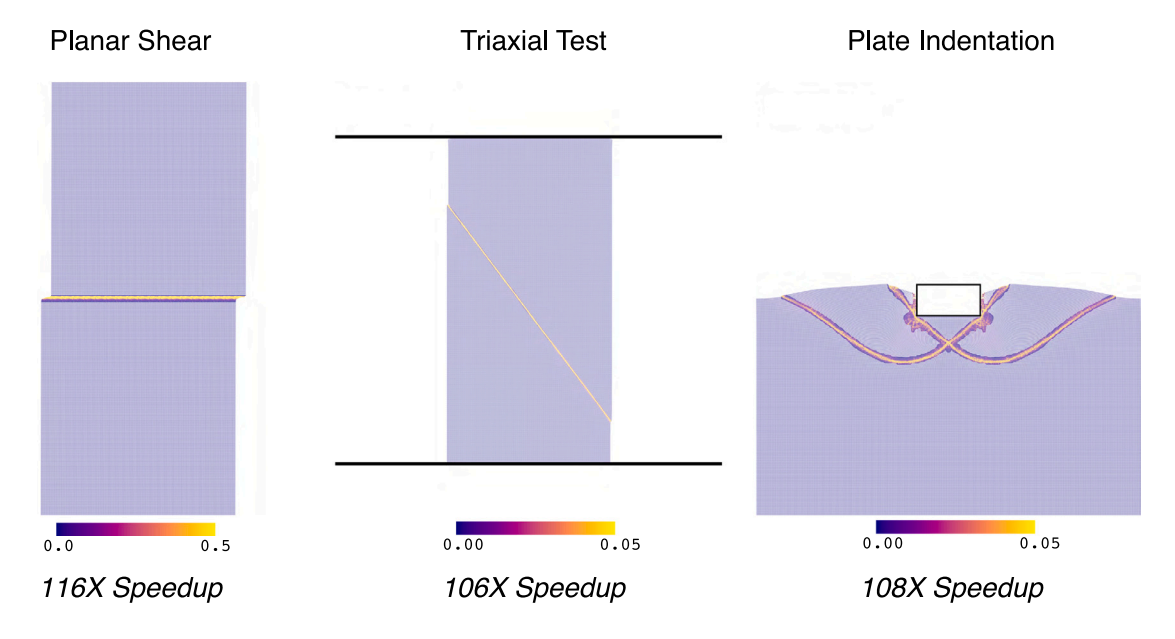


Fig. 26. Over two orders of magnitude performance speedup on large scale examples.

Table 11Large-scale simulations statistics. Since the discrete simulation is too slow to complete, the speedup is computed by comparing the per time step costs for the first 20 discrete time steps.

Experiment	Type	Cell Width	Speedup	Number of Discrete Grains	Total Run Time
Planar Shear	Discrete	n/a	n/a	640,000	n/a
Platiai Sileai	Hybrid	0.75 cm	116X	2,282	Two days
Triaxial	Discrete	n/a	n/a	74,343,046	n/a
Hidaidi	Hybrid	1.5 cm	106X	714,746	One month
Plate Indentation	Discrete	n/a	n/a	63,082,800	n/a
Plate indentation	Hybrid	1.5 cm	108X	469,508	Two weeks

width of $6,000 \ D_{50}$, a fully discrete treatment requires 70 million grains (Table 11). On the contrary, the hybrid simulation requires less than a million discrete grains and is 106 times faster to compute. Notice how the shear band is well-captured by the discrete zone without shearing into the continuum region.

Similar to the triaxial test, no periodicity can be assumed for the large-scale plate indentation test. As shown in Fig. 26 (right), the intruder has a width of 72 cm, entering a pile of granular media that is 13.5 m wide and 4.5 m deep. The hybrid simulation is 108 times faster than a purely discrete simulation, which requires 60 million grains (Table 11).

The total run time is two days for the hybrid planar shear test, one month for the hybrid triaxial test, and two weeks for the hybrid plate indentation. Note that it is impossible to directly compare these results with purely discrete simulations since the purely discrete simulations are too slow to complete; they are expected to take *up to 10 years* on the 32-core computer we use.

Computationally speaking, another benefit of the hybrid approach is the reduction of memory usage due to the reduction of the number of discrete grains. In fact, the memory footprints of the fully discrete triaxial test and the plate indentation test are 156 GB and 84 GB respectively, rendering them impossible to run on average desktops. On the contrary, the hybrid approach consumes only 1 GB and 800 MB of memory respectively, which can be easily satisfied by average laptops, let alone desktops.

6.4.1. Speedup analysis

The speedup of our hybrid approach can be arbitrarily large depending on the setups, as the shear band is roughly codimension-1 in 2D and co-dimension-2 in 3D. In theory, because the hybrid approach only employs the expensive discrete grains in a minuscule portion (O(n)) of the whole domain, the hybrid approach can be arbitrarily faster than the purely discrete approach $(O(n^2))$. The larger the domain is (the larger the n is), the higher the speedup. To systematically quantify this speedup, we conduct an algorithmic analysis.

Suppose that a physical specimen has a height of $T = \mathcal{T}n$ and a width of $W = \mathcal{W}n$ (in 3D, W becomes the cross-sectional area of the specimen: $W = \mathcal{W}n^2$), both in terms of the element size, where n is some dimensionless value. Suppose in addition that a shear band forms in the interior of the domain, crossing the entire width of the specimen with a thickness of T_D , e.g., in the case of planar shear and triaxial test. The total cost of the hybrid simulation comprises three parts: the discrete simulation cost $T_DWN_DC_D$,

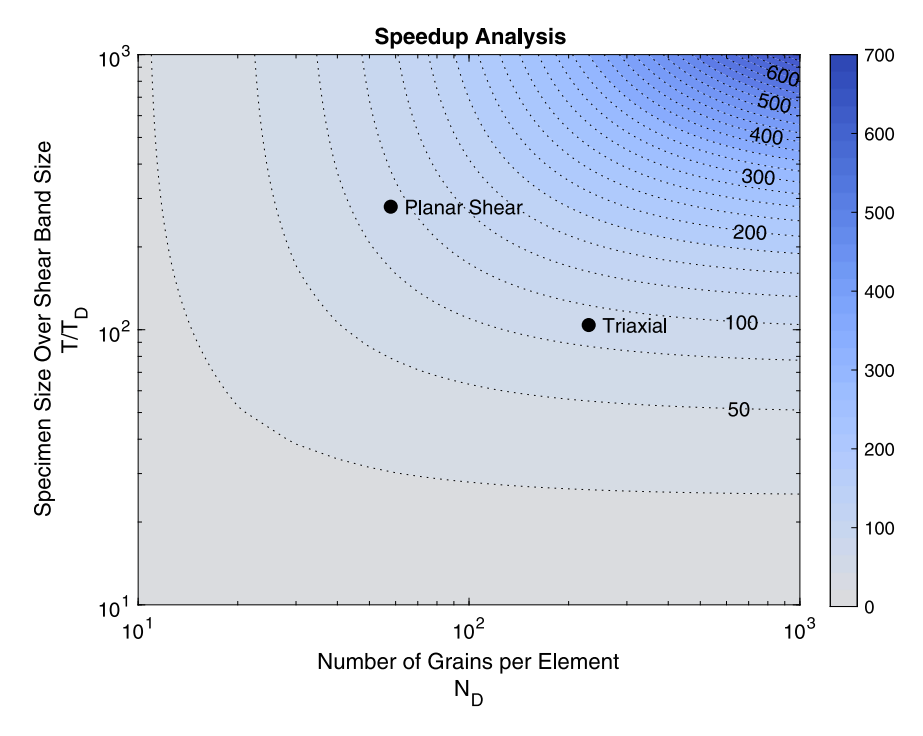


Fig. 27. Speedup analysis of our hybrid approach. Parameters for the analysis are calibrated from actual simulations. The analysis indicates that the large-scale hybrid planar shear and triaxial tests in Table 11 offer a speedup of approximately 100 times, which is consistent with the actual speedup number obtained.

the continuum simulation cost $(T-T_D+2)WC_C$, and the coupling cost $2WC_R$, where N_D is the number of grains per element, C_D is the discrete simulation cost per grain, C_C is the continuum simulation cost per element, C_R is the coupling cost per element, and 2 comes from the fact that the size of the coupling reconciliation zone is two elements wide. Since $T\gg 2$ and $C_R\sim C_C$, the coupling cost is negligible compared to the continuum cost, i.e., the total cost of the hybrid simulation can be estimated as $C^h=T_DWN_DC_D+(T-T_D)WC_C$. In comparison, the total cost of a discrete simulation is $C^d=TWN_DC_D$. Hence, The speedup ratio is obtained by dividing the discrete cost C^d by the hybrid cost C^h :

$$\frac{1}{(\frac{T_D}{T} + (1 - \frac{T_D}{T})\frac{C_C}{C_D N_D})}.$$

In our work, $C_D=1.14\times10^{-6}$ s, $C_C=4.87\times10^{-7}$ s, $N_D=230$ for the triaxial test, and $N_D=58$ for the planar shear test. Fig. 27 shows a plot of the speedup ratio in terms of N_D and T/T_D . Both N_D and T/T_D correlated positively with the speedup ratio, i.e., the higher the number of grains per element, the higher the speedup; the thinner the shear band is compared to the height of the domain, the higher the speedup. Nevertheless, the number of grains per element cannot be chosen arbitrarily and should be chosen such that the continuum simulation remains valid.

For the regimes where our experiments reside, the continuum simulation cost $(T - T_D)C_C$ is only a fraction (24%) of the discrete simulation cost $T_DN_DC_D$. Therefore, $C^h = 1.24T_DWnN_DC_D = O(n)$ while $C^d = TnWnN_DC_D = O(n^2)$.

Note that we assume a linear scaling, i.e., the cost of discrete simulation varies linearly with the number of grains. In practice, due to memory and cache limits, when simulating a large number of discrete grains, the pure discrete approach often suffers from a further slow down; the hybrid approach, on the contrary, does not tend to suffer from this slow down because the hybrid approach is rather memory friendly: instead of simulating N_D grains per element, the hybrid approach only needs to simulate one element. Therefore, in these large scale regimes, the hybrid approach offers an even higher speedup advantage than the prediction by the theoretical analysis. It is also worth noting that while this particular analysis is conducted for the shear band arising from the planar shear-like and the triaxial-like experiments, a similar result is expected from shear bands arising from the plate indentation-like experiments where the localized shear band remains a minuscule portion of the simulation domain.

7. Conclusions and future work

In this work, we introduce the hybrid discrete-continuum approach as a new concurrent multiscale modeling tool for shear localization. Employing an adaptive domain partition technique, a careful discrete enrichment procedure with kinematic training, and a robust discrete-continuum integrator, the hybrid approach combines the accurate-yet-slow discrete model and the fast-yet-less-precise continuum model with the aim of achieving the best of both worlds: a fast simulation framework that excels at capturing

the post-localization shear banding dynamics. Quantitative agreements are observed between the hybrid approach and the pure discrete simulation in terms of both the shear band thickness as well as the stress response. The hybrid method achieves this accuracy with as much as a 100 times reduction in computational cost. Requiring zero prior knowledge of the shear band and avoiding the complexities of a nonlocal model, the hybrid approach is also shown to be free from mesh dependence issues that often plague continuum simulations. Moreover, the hybrid approach produces consistent results under enrichment parameter perturbation.

In the future, we intend to explore other real-world geometries that induce shear localization of granular media, e.g., the geo-scale fault slip problem. Additionally, we aim to explore situations where the shear band constantly evolves, such as plate indentation with a deeply inserted plate as well as industrial problems such as that of a bulldozer pushing gravel. Extension of existing shear bands and homogenization of older shear bands will be necessary to achieve maximum accuracy and speedup. With a routine that can extend the discrete domain after a designated shear band has been enriched, we may also be able to be more conservative with the amount of grains we enrich in the first place, i.e., using a smaller ϕ_0 , without loss of fidelity in representing the physical shear band. Furthermore, future work includes going beyond shear bands to study other granular flow scenarios with the hybrid method. Particularly, we intend to further validate and extend the kinematic training algorithm proposed in this paper as a general enrichment methodology for creating discrete packings that agree with the characteristics of a continuum region.

CRediT authorship contribution statement

Peter Yichen Chen: Research, Formal analysis, Writing - original draft. **Maytee Chantharayukhonthorn:** Research, Formal analysis, Writing - original draft. **Yonghao Yue:** Research, Formal analysis, Writing - original draft. **Eitan Grinspun:** Research, Formal analysis, Writing - original draft.

Declaration of competing interest

The authors declare that they have no known competing financial interests or personal relationships that could have appeared to influence the work reported in this paper.

Acknowledgments

We thank Breannan Smith for contributing to the code base. We thank Steve WaiChing Sun, Kun Wang, and Shashank Agarwal for insightful discussions. This work was supported in part by the National Science Foundation, USA (Grants CBET-17-06689, CBET-17-06193) and the JSPS Grant-in-Aid for Young Scientists (A) 17H04682.

Appendix A. Details of shear band analysis

To quantitatively measure the thickness of the shear band, we first compute the Cundall's best-fit strain ϵ^c for each discrete grain (Bagi, 2006; Kawamoto et al., 2018). Given N number of grains, dx_i and dX_i for $i = 1 \cdots N$ are defined to be the deviation of grain i from the center of this group of grains in the current and reference configuration, respectively. Then the Cundall's best-fit displacement gradient ∇u^c can be defined as

$$\min_{\nabla \boldsymbol{u}^c} \frac{1}{2} \sum_{i} \|d\boldsymbol{u}_i - \nabla \boldsymbol{u}^c d\boldsymbol{X}_i\|^2,$$

where $d\mathbf{u}_i = d\mathbf{x}_i - d\mathbf{X}_i$ and Cundall's best-fit strain is $\epsilon^c = \frac{1}{2}(\nabla \mathbf{u}^c + \nabla \mathbf{u}^{cT})$.

To apply Cundall's best-fit strain, we triangulate the grains using a standard Delaunay triangulation package (Shewchuk, 1996). For each grain i, we then compute its ϵ^c by applying the Cundall's best-fit strain formula to the grain centroid and its neighboring centroids from triangulation. Finally, to highlight the shear flow, we compute the deviatoric part of ϵ^c as $\epsilon^c_d = \epsilon^c - \frac{1}{2} \text{tr}[\epsilon^c]I$.

Figs. 11, 18 and 24 demonstrate the magnitude of incremental ϵ_d^c for grains in both the discrete simulation and hybrid simulation. Notice how for both discrete and continuum simulations, intensive strain is localized into a thin region in the middle of the specimen.

We then identify the grains in the shear band by choosing grains whose deviatoric strain is beyond the 98th percentile of all the grains in the pure discrete simulation. After removing the outliers (grains whose distance from the center of the shear band is larger than two standard deviations), we compute a minimum-area bounding box for the shear band grains to get the thickness t_s of the shear band.

Appendix B. Details of applying the confining pressure

One challenge of numerically modeling the triaxial test is how to apply the confining pressure. An elastic membrane is used in the physical experiment to hold the grains, and the specimen is placed in a container of fluid that asserts the confining pressure on the elastic membrane, thereby asserting pressure on the grains (Wood, 1990).

To numerically model the elastic membrane in the triaxial test, we introduce a mass-spring based elastic membrane and discretize it through the MPM background grid using the approach of Jiang et al. (2015) where a FEM elastic membrane is coupled to MPM non-Newtonian flow. Discretizing through the background grid allows natural coupling between the elastic membrane and the MPM

Table B.1 Membrane parameters.

Parameters	Value	Unit
k _{ms}	10,000	N/m
γ_{ms}	1	N·s/m

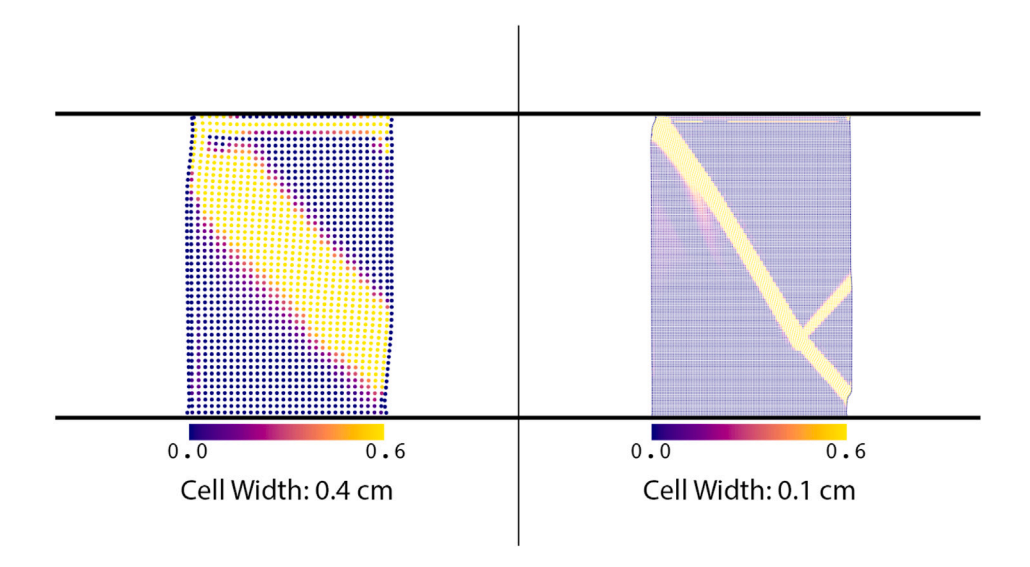


Fig. C.1. Continuum triaxial loading with different mesh resolutions: low resolution (left) and high resolution (right). The simulation is colored by the magnitude of plastic strain rate $\|\dot{e}^p\|$. Strong mesh dependence is observed as the one with lower resolution has a thicker shear band.

granular media. The values for the mass-spring system's stiffness k_{ms} and damping coefficient γ_{ms} are listed in Table B.1. To best mimic the physical elastic membrane, the numerical membrane is pre-loaded with tensile stress at the beginning of the simulation.

With this numerical elastic membrane in place, we can apply the confining pressure in the normal direction to the membrane. This mass-spring based elastic membrane is also used to enforce the confining pressure for the discrete simulation as well as the hybrid simulation. The elastic membrane naturally couples with the discrete grains through the hybridization algorithm discussed in Section 5. No extra implementation is needed, and no discrete-grain based elastic membrane is needed.

Appendix C. Mesh dependence of the continuum model

While the continuum model can *qualitatively* model the formation of a shear band, by no means does it give us a *quantitative* model of the shear band in the post localization regime. Due to the lack of intrinsic length scale in the continuum model, it effectively chooses the discretization grid resolution to be its length scale. As demonstrated in Fig. C.1, larger background grid cell width, i.e., lower resolution, results in a thicker shear band.

Appendix D. Mesh independence of the hybrid oracle

As shown in Fig. D.1, when using D_{50} as the sole length scale in shear band detection, the oracle fails to detect the shear band in the low-resolution simulation whose strain rate Laplacian never hits the threshold. Alternatively, by using both ΔX , the element size, and D_{50} as the thresholding length scales, our oracle detects shear band in both high resolution and low-resolution meshes.

Appendix E. Rate independence of the hybrid oracle

Fig. E.1 demonstrates the oracle's rate independence. The oracle detects and enriches the continuum shear band in both the fast and slow scenarios under different geometries.

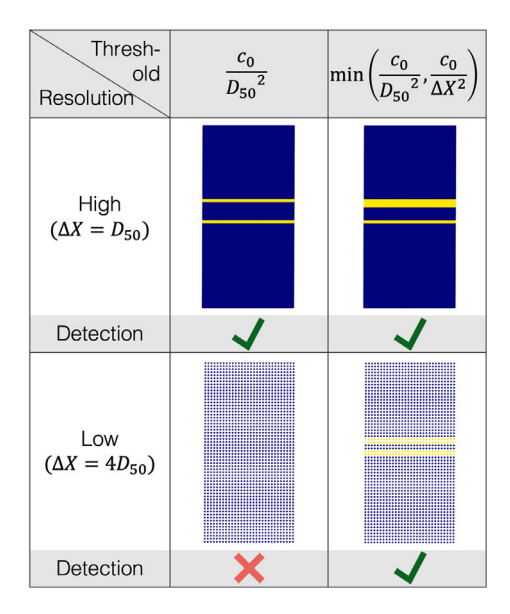


Fig. D.1. Mesh independence of the hybrid oracle. In the over-consolidated, planar shear test, shear localizes in the middle of the domain, in both the high resolution and the low-resolution simulations. Using both the grain size and the element size as the thresholding length scales leads to mesh independent shear band detection (yellow region) while using the grain size alone fails to detect the shear band in the low-resolution simulation.

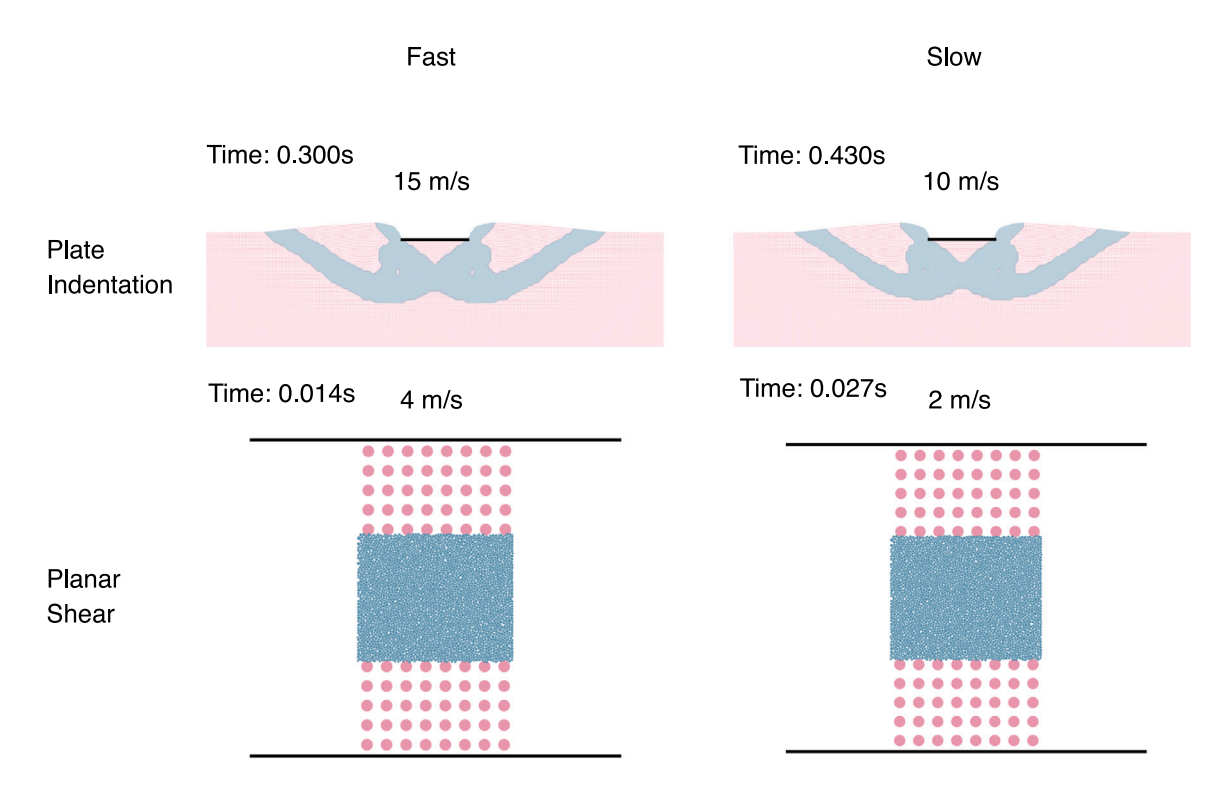


Fig. E.1. The moment the hybrid simulation enriches the continuum shear band into the discrete shear band across different flow velocities and boundary conditions (top row: indentation; bottom row: planar shear). The hybrid oracle flags the same shear band locations under both fast and slow flows, with the faster flow being enriched earlier. Velocities of the top plate are marked.

Appendix F. Dimensional analysis of shear band thickness

Letting T_s be the thickness of the shear band, we seek its reliance on several independent state variables of the granular specimen: void ratio e, friction coefficient μ , mean grain diameter d [m], particle stiffness k_n [N/m], total mass m [kg], height H [m], width

L [m], confining pressure P [N/m²], number of Particles N. Therefore

$$T_s = T_s(e, \mu, d, k_n, m, H, L, P, N).$$

Let d be the unit of measure for length, m be the unit of measure for mass, and $\sqrt{\frac{m}{dP}}$ be the unit of measure for time. We have the following dimensionless variables: e, μ , $\frac{k_n}{Pd}$, $\frac{H}{d}$, and N. By the Buckingham π theorem, the dimensionless shear band thickness $\mathcal{T}_s = \frac{T_s}{d}$ is associated to these dimensionless state variables by

$$\mathcal{T}_s = \mathcal{T}_s(e, \mu, \frac{k_n}{Pd}, \frac{H}{d}, \frac{L}{d}, N).$$

Consequently, the shear band thickness remains constant if k_n and P are scaled by the same factor.

References

Abe, K., Soga, K., Bandara, S., 2013. Material point method for coupled hydromechanical problems. J. Geotech. Geoenviron. Eng. 140 (3), 04013033.

Agarwal, S., Karsai, A., Goldman, D.I., Kamrin, K., 2020. Surprising simplicity in the modeling of dynamic granular intrusion, arXiv e-prints, arXiv-2005.

Agarwal, S., Karsai, A., Goldman, D.I., Kamrin, K., 2021. Efficacy of simple continuum models for diverse granular intrusions, arXiv preprint arXiv:2101.10321.

Agarwal, S., Senatore, C., Zhang, T., Kingsbury, M., Iagnemma, K., Goldman, D.I., Kamrin, K., 2019a. Modeling of the interaction of rigid wheels with dry granular media. J. Terramech. 85, 1-14.

Aifantis, E.C., 1984. On the microstructural origin of certain inelastic models.

Alsaleh, M.I., Voyiadjis, G.Z., Alshibli, K.A., 2006. Modelling strain localization in granular materials using micropolar theory: mathematical formulations. Int. J. Numer. Anal. Methods Geomech. 30 (15), 1501–1524.

Alshibli, K.A., Alsaleh, M.I., Voyiadjis, G.Z., 2006. Modelling strain localization in granular materials using micropolar theory: Numerical implementation and verification. Int. J. Numer. Anal. Methods Geomech. 30 (15), 1525–1544.

Alshibli, K.A., Sture, S., 1999. Sand shear band thickness measurements by digital imaging techniques. J. Comput. Civil Eng. 13 (2), 103-109.

Anand, L., Aslan, O., Chester, S.A., 2012. A large-deformation gradient theory for elastic-plastic materials: strain softening and regularization of shear bands. Int. J. Plast. 30, 116–143.

Anand, L., Gu, C., 2000. Granular materials: constitutive equations and strain localization. J. Mech. Phys. Solids 48 (8), 1701-1733.

Anand, L., Spitzig, W., 1980. Initiation of localized shear bands in plane strain. J. Mech. Phys. Solids 28 (2), 113-128.

Anciaux, G., Junge, T., Hodapp, M., Cho, J., Molinari, J.-F., Curtin, W., 2018. The coupled atomistic/discrete-dislocation method in 3d part I: Concept and algorithms. J. Mech. Phys. Solids 118, 152–171.

Andersen, S., Andersen, L., 2010. Modelling of landslides with the material-point method. Comput. Geosci. 14 (1), 137-147.

Anderson, T.B., Jackson, R., 1967. Fluid mechanical description of fluidized beds. Equations of motion. Ind. Eng. Chem. Fundam. 6 (4), 527-539.

Andrade, J.E., Avila, C., Hall, S., Lenoir, N., Viggiani, G., 2011. Multiscale modeling and characterization of granular matter: from grain kinematics to continuum mechanics. J. Mech. Phys. Solids 59 (2), 237–250.

Andrade, J.E., Tu, X., 2009. Multiscale framework for behavior prediction in granular media. Mech. Mater. 41 (6), 652-669.

Askari, H., Kamrin, K., 2016. Intrusion rheology in grains and other flowable materials. Nat. Mater. 15 (12), 1274.

Bagi, K., 2006. Analysis of microstructural strain tensors for granular assemblies. Int. J. Solids Struct. 43 (10), 3166-3184.

Bardenhagen, S., Brackbill, J., Sulsky, D., 2000. The material-point method for granular materials. Comput. Methods Appl. Mech. Engrg. 187 (3-4), 529-541.

Bardet, J.-P., Proubet, J., 1991. A numerical investigation of the structure of persistent shear bands in granular media. Geotechnique 41 (4), 599-613.

Bardet, J.-P., Proubet, J., 1992. Shear-band analysis in idealized granular material. J. Eng. Mech. 118 (2), 397-415.

Batra, R., Kim, C., 1991. Effect of thermal conductivity on the initiation, growth and bandwidth of adiabatic shear bands. Internat. J. Engrg. Sci. 29 (8), 949-960.

Bažant, Z.P., Belytschko, T.B., Chang, T.-P., 1984. Continuum theory for strain-softening. J. Eng. Mech. 110 (12), 1666-1692.

Bažant, Z.P., Lin, F.-B., 1988. Non-local yield limit degradation. Internat. J. Numer. Methods Engrg. 26 (8), 1805-1823.

Beeler, N., Tullis, T., Blanpied, M., Weeks, J., 1996. Frictional behavior of large displacement experimental faults. J. Geophys. Res.: Solid Earth 101 (B4), 8697–8715.

Belytschko, T., Bažant, Z.P., Yul-Woong, H., Ta-Peng, C., 1986. Strain-softening materials and finite-element solutions. Comput. Struct. 23 (2), 163-180.

Belytschko, T., Fish, J., Engelmann, B.E., 1988. A finite element with embedded localization zones. Comput. Methods Appl. Mech. Engrg. 70 (1), 59-89.

Bigoni, D., Hueckel, T., 1991. Uniqueness and localization? i. associative and non-associative elastoplasticity. Int. J. Solids Struct. 28 (2), 197-213.

Bocquet, L., Losert, W., Schalk, D., Lubensky, T., Gollub, J., 2001. Granular shear flow dynamics and forces: Experiment and continuum theory. Phys. Rev. E 65 (1), 011307.

Borst, R.d., Sluys, L.J., Muhlhaus, H.-B., Pamin, J., 1993. Fundamental issues in finite element analyses of localization of deformation. Eng. Comput.: Int. J. Comput.-Aided Eng. 10 (2), 99–121.

Chambon, G., Schmittbuhl, J., Corfdir, A., 2006. Frictional response of a thick gouge sample: 1. Mechanical measurements and microstructures. J. Geophys. Res.: Solid Earth 111 (B9).

Chang, C., Askes, H., Sluys, L., 2002. Higher-order strain/higher-order stress gradient models derived from a discrete microstructure, with application to fracture. Eng. Fract. Mech. 69 (17), 1907–1924.

Chantharayukhonthorn, M., 2019. A Hybrid Discrete Element and Continuum Method for Multiscale Granular Media Modeling (Master's thesis). Massachusetts Institute of Technology.

Chen, Q., 2011. Multiscale Modeling of Failure in Granular Media: From Continuum Scales to Granular Scale. Northwestern University.

Chen, J.-S., Wu, C.-T., Belytschko, T., 2000. Regularization of material instabilities by meshfree approximations with intrinsic length scales. Internat. J. Numer. Methods Engrg. 47 (7), 1303–1322.

Cho, J., Molinari, J.-F., Curtin, W.A., Anciaux, G., 2018. The coupled atomistic/discrete-dislocation method in 3d. Part III: dynamics of hybrid dislocations. J. Mech. Phys. Solids 118, 1–14.

Christoffersen, J., Mehrabadi, M.M., Nemat-Nasser, S., 1981. A micromechanical description of granular material behavior. J. Appl. Mech. 48 (2), 339-344.

Cundall, P.A., 1989. Numerical experiments on localization in frictional materials. Ingenieur-archiv 59 (2), 148-159.

Cundall, P.A., Strack, O.D., 1979. A discrete numerical model for granular assemblies. Geotechnique 29 (1), 47-65.

Da Cruz, F., Emam, S., Prochnow, M., Roux, J.-N., Chevoir, F., 2005. Rheophysics of dense granular materials: Discrete simulation of plane shear flows. Phys. Rev. E 72 (2), 021309.

Daub, E.G., Carlson, J.M., 2010. Friction, fracture, and earthquakes. Annu. Rev. Condens. Matter Phys. 1 (1), 397-418.

Daviet, G., Bertails-Descoubes, F., 2016. A semi-implicit material point method for the continuum simulation of granular materials. ACM Trans. Graph. 35 (4), 102:1–102:13.

Davydov, D., Pelteret, J.-P., Steinmann, P., 2014. Comparison of several staggered atomistic-to-continuum concurrent coupling strategies. Comput. Methods Appl. Mech. Engrg. 277, 260–280.

De Borst, R., Mühlhaus, H.-B., 1992. Gradient-dependent plasticity: formulation and algorithmic aspects. Internat. J. Numer. Methods Engrg. 35 (3), 521-539.

De Borst, R., Pamin, J., Peerlings, R., Sluys, L., 1995. On gradient-enhanced damage and plasticity models for failure in quasi-brittle and frictional materials. Comput. Mech. 17 (1–2), 130–141.

Desrues, J., Viggiani, G., 2004. Strain localization in sand: an overview of the experimental results obtained in grenoble using stereophotogrammetry. Int. J. Numer. Anal. Methods Geomech. 28 (4), 279–321.

Dhia, H.B., 1998. Multiscale mechanical problems: the arlequin method. C. R. Acad. Sci., Paris II 12 (326), 899-904.

Drucker, D.C., Prager, W., 1952. Soil mechanics and plastic analysis or limit design. Q. Appl. Math. 10 (2), 157-165.

Dunatunga, S., Kamrin, K., 2015. Continuum modelling and simulation of granular flows through their many phases. J. Fluid Mech. 779, 483-513.

Dunatunga, S., Kamrin, K., 2017. Continuum modeling of projectile impact and penetration in dry granular media. J. Mech. Phys. Solids 100, 45-60.

Engelen, R., Fleck, N., Peerlings, R., Geers, M., 2006. An evaluation of higher-order plasticity theories for predicting size effects and localisation. Int. J. Solids Struct. 43 (7–8), 1857–1877.

Engelen, R.A., Geers, M.G., Baaijens, F.P., 2003. Nonlocal implicit gradient-enhanced elasto-plasticity for the modelling of softening behaviour. Int. J. Plasticity 19 (4), 403–433.

Eringen, A.C., 1966. Theory of micropolar fluids. J. Math. Mech. 1-18.

Eringen, A.C., 1981. On nonlocal plasticity. Internat. J. Engrg. Sci. 19 (12), 1461-1474.

Finno, R.J., Harris, W., Mooney, M.A., Viggiani, G., 1997. Shear bands in plane strain compression of loose sand. Geotechnique 47 (1), 149-165.

Fish, J., 2013. Practical Multiscaling. John Wiley & Sons.

Gao, M., Pradhana, A., Han, X., Guo, Q., Kot, G., Sifakis, E., Jiang, C., 2018. Animating fluid sediment mixture in particle-laden flows. ACM Trans. Graph. 37 (4), 149:1–149:11.

Ghareeb, A., Elbanna, A., 2020. An adaptive quasicontinuum approach for modeling fracture in networked materials: Application to modeling of polymer networks.

J. Mech. Phys. Solids 137, 103819.

Goldman, D.I., Umbanhowar, P., 2008. Scaling and dynamics of sphere and disk impact into granular media. Phys. Rev. E 77 (2), 021308.

Gu, X., Huang, M., Qian, J., 2014. Discrete element modeling of shear band in granular materials. Theor. Appl. Fract. Mech. 72, 37-49.

Guo, P., 2012. Critical length of force chains and shear band thickness in dense granular materials. Acta Geotech. 7 (1), 41-55.

Guo, N., Zhao, J., 2014. A coupled FEM/DEM approach for hierarchical multiscale modelling of granular media. Internat. J. Numer. Methods Engrg. 99 (11), 789–818.

Guo, N., Zhao, J., 2016a. 3D multiscale modeling of strain localization in granular media. Comput. Geotech. 80, 360-372.

Guo, N., Zhao, J., 2016b. Multiscale insights into classical geomechanics problems. Int. J. Numer. Anal. Methods Geomech. 40 (3), 367-390.

Han, C., Drescher, A., 1993. Shear bands in biaxial tests on dry coarse sand. Soils Found. 33 (1), 118-132.

Hencky, H., 1933. The elastic behavior of vulcanized rubber. Rubber Chem. Technol. 6 (2), 217-224.

Hill, R., 1963. Elastic properties of reinforced solids: some theoretical principles. J. Mech. Phys. Solids 11 (5), 357-372.

Hodapp, M., Anciaux, G., Molinari, J.-F., Curtin, W., 2018. Coupled atomistic/discrete dislocation method in 3D Part II: Validation of the method. J. Mech. Phys. Solids 119, 1–19.

Hu, N., Molinari, J., 2004. Shear bands in dense metallic granular materials. J. Mech. Phys. Solids 52 (3), 499-531.

Iwashita, K., Oda, M., 1998. Rolling resistance at contacts in simulation of shear band development by DEM. J. Eng. Mech. 124 (3), 285-292.

Iwashita, K., Oda, M., 2000. Micro-deformation mechanism of shear banding process based on modified distinct element method. Powder Technol. 109 (1–3), 192–205.

Jaeger, H.M., 2015. Celebrating soft matter's 10th anniversary: Toward jamming by design. Soft Matter 11 (1), 12-27.

Jaeger, H.M., Nagel, S.R., Behringer, R.P., 1996. Granular solids, liquids, and gases. Rev. Modern Phys. 68 (4), 1259.

Jiang, M., Leroueil, S., Konrad, J.-M., 2005. Yielding of microstructured geomaterial by distinct element method analysis. J. Eng. Mech. 131 (11), 1209-1213.

Jiang, Y., Li, M., Jiang, C., Alonso-marroquin, F., 2019. A hybrid material-point spheropolygon-element method for solid and granular material interaction. arXiv preprint arXiv:1909.13655.

Jiang, C., Schroeder, C., Selle, A., Teran, J., Stomakhin, A., 2015. The affine particle-in-cell method. ACM Trans. Graph. 34 (4), 51:1-51:10.

Jiang, M., Yu, H.-S., Leroueil, S., 2007. A simple and efficient approach to capturing bonding effect in naturally microstructured sands by discrete element method. Internat. J. Numer. Methods Engrg. 69 (6), 1158–1193.

Jun, S., Im, S., 2000. Multiple-scale meshfree adaptivity for the simulation of adiabatic shear band formation. Comput. Mech. 25 (2-3), 257-266.

Kamrin, K., 2019. Non-locality in Granular Flow: Phenomenology and modeling approaches. Front. Phys. 7, 116.

Kamrin, K., Koval, G., 2014. Effect of particle surface friction on nonlocal constitutive behavior of flowing granular media. Comput. Part. Mech. 1 (2), 169–176. Kang, W., Feng, Y., Liu, C., Blumenfeld, R., 2018. Archimedes' law explains penetration of solids into granular media. Nat. Commun. 9 (1), 1101.

Kawamoto, R., Andò, E., Viggiani, G., Andrade, J.E., 2018. All you need is shape: Predicting shear banding in sand with LS-DEM. J. Mech. Phys. Solids 111, 375–392.

Kiriyama, T., 2016. Numerical study of shear band formation in triaxial compression tests. Japan. Geotech. Soc. Special Publ. 2 (18), 697-702.

Klár, G., Gast, T., Pradhana, A., Fu, C., Schroeder, C., Jiang, C., Teran, J., 2016. Drucker-prager elastoplast. sand animat.. ACM Trans. Graph. 35 (4), 103:1–103:20. Kuhn, M.R., 2017. 4 - loading, movement, and strength. In: Kuhn, M.R. (Ed.), Granular Geomechanics. Elsevier, pp. 153–227.

LeMonds, J., Needleman, A., 1986. An Analysis of Shear Band Development Incorporating Heat Conduction. Tech. Rep., Brown Univ Providence Ri Div of Engineering.

Lemonds, J., Needleman, A., 1986. Finite element analyses of shear localization in rate and temperature dependent solids. Mech. Mater. 5 (4), 339-361.

Li, S., Liu, W.K., 2000. Numerical simulations of strain localization in inelastic solids using mesh-free methods. Internat. J. Numer. Methods Engrg. 48 (9), 1285–1309.

Liang, W., Zhao, J., 2019. Multiscale modeling of large deformation in geomechanics. Int. J. Numer. Anal. Methods Geomech. 43 (5), 1080-1114.

Liu, W.K., Karpov, E., Zhang, S., Park, H., 2004. An introduction to computational nanomechanics and materials. Comput. Methods Appl. Mech. Engrg. 193 (17–20), 1529–1578.

Liu, W.K., Park, H.S., Qian, D., Karpov, E.G., Kadowaki, H., Wagner, G.J., 2006. Bridging scale methods for nanomechanics and materials. Comput. Methods Appl. Mech. Engrg. 195 (13–16), 1407–1421.

Liu, C., Sun, W., 2019. Shift boundary material point method: an image-to-simulation workflow for solids of complex geometries undergoing large deformation. Comput. Part. Mech. 1–18.

Liu, C., Sun, W., 2020. ILS-Mpm: an implicit level-set-based material point method for frictional particulate contact mechanics of deformable particles. arXiv preprint arXiv:2001.02412.

Liu, C., Sun, Q., Yang, Y., 2017. Multi-scale modelling of granular pile collapse by using material point method and discrete element method. Procedia Eng. 175 29–35

Liu, Y., Sun, W., Yuan, Z., Fish, J., 2016. A nonlocal multiscale discrete-continuum model for predicting mechanical behavior of granular materials. Internat. J. Numer. Methods Engrg. 106 (2), 129–160.

Mandel, J., Dantu, P., 1963. Contribution À L'étude Théorique et Expérimentale Du Coefficient d'élastcité D'un Milieu Hétérogène, Mais Statistiquement Homogène, Par J. Mandel et P. Dantu.

Mandl, G., De Jong, L., Maltha, A., 1977. Shear zones in granular material. Rock Mech. 9 (2-3), 95-144.

Mast, C.M., Arduino, P., Mackenzie-Helnwein, P., Miller, G.R., 2015. Simulating granular column collapse using the material point method. Acta Geotech. 10

Mehrabadi, M., Cowin, S., 1978. Initial planar deformation of dilatant granular materials. J. Mech. Phys. Solids 26 (4), 269-284.

Miller, R.E., Tadmor, E.B., 2002. The quasicontinuum method: Overview, applications and current directions. J. Comput.-Aided Mater. Des. 9 (3), 203-239.

Moreau, J.J., 1988. Unilateral contact and dry friction in finite freedom dynamics. In: Nonsmooth Mechanics and Applications. Springer, pp. 1-82.

Mühlhaus, H.-B., Alfantis, E., 1991. A variational principle for gradient plasticity. Int. J. Solids Struct. 28 (7), 845-857.

Mühlhaus, H.-B., Vardoulakis, I., 1987. The thickness of shear bands in granular materials. Geotechnique 37 (3), 271-283.

Needleman, A., 1988. Material rate dependence and mesh sensitivity in localization problems. Comput. Methods Appl. Mech. Engrg. 67 (1), 69-85.

Nemes, J., Speciel, E., 1996. Use of a rate-dependent continuum damage model to describe strain-softening in laminated composites. Comput. Struct. 58 (6), 1083–1092

Oda, M., Iwashita, K., 2000. Study on couple stress and shear band development in granular media based on numerical simulation analyses. Int. J. Eng. Sci. 38 (15), 1713–1740.

Oda, M., Kazama, H., 1998. Microstructure of shear bands and its relation to the mechanisms of dilatancy and failure of dense granular soils. Geotechnique 48 (4), 465–481.

O'Hern, C.S., Langer, S.A., Liu, A.J., Nagel, S.R., 2002. Random packings of frictionless particles. Phys. Rev. Lett. 88 (7), 075507.

Ortiz, M., Ouigley IV, J., 1991, Adaptive mesh refinement in strain localization problems, Comput, Methods Appl, Mech. Engrg. 90 (1-3), 781-804.

Pietruszczak, S., Mroz, Z., 1981. Finite element analysis of deformation of strain-softening materials. Internat. J. Numer. Methods Engrg. 17 (3), 327-334.

Poh, L., Peerlings, R., Geers, M., Swaddiwudhipong, S., 2011. An implicit tensorial gradient plasticity model–formulation and comparison with a scalar gradient model. Internat. J. Solids Struct. 48 (18), 2595–2604.

Qian, D., Liu, W.K., Zheng, Q., 2008. Concurrent quantum/continuum coupling analysis of nanostructures. Comput. Methods Appl. Mech. Engrg. 197 (41–42), 3291–3323.

Qian, D., Wagner, G.J., Liu, W.K., 2004. A multiscale projection method for the analysis of carbon nanotubes. Comput. Methods Appl. Mech. Engrg. 193 (17–20), 1603–1632.

Rice, J.R., 1975. On the stability of dilatant hardening for saturated rock masses. J. Geophys. Res. 80 (11), 1531-1536.

Roscoe, K.H., 1970. The influence of strains in soil mechanics. Geotechnique 20 (2), 129-170.

Rudnicki, J.W., Rice, J., 1975. Conditions for the localization of deformation in pressure-sensitive dilatant materials. J. Mech. Phys. Solids 23 (6), 371-394.

Rycroft, C.H., Kamrin, K., Bazant, M.Z., 2009. Assessing continuum postulates in simulations of granular flow. J. Mech. Phys. Solids 57 (5), 828-839.

Semnani, S.J., White, J.A., Borja, R.I., 2016. Thermoplasticity and strain localization in transversely isotropic materials based on anisotropic critical state plasticity. Int. J. Numer. Anal. Methods Geomech. 40 (18), 2423–2449.

Shewchuk, J.R., 1996. Triangle: Engineering a 2D quality mesh generator and delaunay triangulator. In: Workshop on Applied Computational Geometry. Springer, pp. 203–222.

Shilkrot, L., Miller, R.E., Curtin, W.A., 2004. Multiscale plasticity modeling: coupled atomistics and discrete dislocation mechanics. J. Mech. Phys. Solids 52 (4), 755–787.

Sluys, L., De Borst, R., 1992. Wave propagation and localization in a rate-dependent cracked medium—model formulation and one-dimensional examples. Int. J. Solids Struct. 29 (23), 2945–2958.

Sluys, L., De Borst, R., Mühlhaus, H.-B., 1993. Wave propagation, localization and dispersion in a gradient-dependent medium. Int. J. Solids Struct. 30 (9), 1153–1171.

Sokolovskii, V.V., 1965, Statics of Granular Media, Pergamon Press,

de Souza Neto, E.A., Peric, D., Owen, D.R., 2011. Computational Methods for Plasticity: Theory and Applications. John Wiley & Sons.

Sulsky, D., Zhou, S.-J., Schreyer, H.L., 1995. Application of a particle-in-cell method to solid mechanics. Comput. Phys. Commun. 87 (1-2), 236-252.

Sun, W., Kuhn, M.R., Rudnicki, J.W., 2013. A multiscale DEM-LBM analysis on permeability evolutions inside a dilatant shear band. Acta Geotech. 8 (5), 465–480.

Tadmor, E.B., Ortiz, M., Phillips, R., 1996a. Quasicontinuum analysis of defects in solids. Phil. Mag. A 73 (6), 1529-1563.

Tadmor, E.B., Phillips, R., Ortiz, M., 1996b. Mixed atomistic and continuum models of deformation in solids. Langmuir 12 (19), 4529-4534.

Tampubolon, A.P., Gast, T., Klár, G., Fu, C., Teran, J., Jiang, C., Museth, K., 2017. Multi-species simulation of porous sand and water mixtures. ACM Trans. Graph. 36 (4), 105:1–105:11.

Towhata, I., 2008. Geotechnical Earthquake Engineering. Springer Science & Business Media.

Tu, X., Andrade, J.E., Chen, Q., 2009. Return mapping for nonsmooth and multiscale elastoplasticity. Comput. Methods Appl. Mech. Engrg. 198 (30-32), 2286-2296

Vardoulakis, I., 1998. Strain localization in granular materials. In: Behaviour of Granular Materials. Springer, pp. 339-400.

Wagner, G.J., Liu, W.K., 2003. Coupling of atomistic and continuum simulations using a bridging scale decomposition. J. Comput. Phys. 190 (1), 249-274.

Wallin, M., Curtin, W., Ristinmaa, M., Needleman, A., 2008. Multi-scale plasticity modeling: Coupled discrete dislocation and continuum crystal plasticity. J. Mech. Phys. Solids 56 (11), 3167–3180.

Weisstein, E.W., 2003. Logistic Equation. Wolfram Research, Inc.

Wellmann, C., Wriggers, P., 2012. A two-scale model of granular materials. Comput. Methods Appl. Mech. Engrg. 205, 46-58.

Wood, D.M., 1990. Soil Behaviour and Critical State Soil Mechanics. Cambridge University Press.

Xiao, S., Belytschko, T., 2004. A bridging domain method for coupling continua with molecular dynamics. Comput. Methods Appl. Mech. Engrg. 193 (17–20), 1645–1669.

Yan, B., Regueiro, R.A., Sture, S., 2010. Three-dimensional ellipsoidal discrete element modeling of granular materials and its coupling with finite element facets. Eng. Comput..

Yang, Y., Misra, A., 2012. Micromechanics based second gradient continuum theory for shear band modeling in cohesive granular materials following damage elasticity. Int. J. Solids Struct. 49 (18), 2500–2514.

Yue, Y., Smith, B., Batty, C., Zheng, C., Grinspun, E., 2015. Continuum foam: A material point method for shear-dependent flows. ACM Trans. Graph. 34 (5), 160:1–160:20.

Yue, Y., Smith, B., Chen, P.Y., Chantharayukhonthorn, M., Kamrin, K., Grinspun, E., 2018. Hybrid grains: Adaptive coupling of discrete and continuum simulations of granular media. ACM Trans. Graph. 37 (6), 283:1–283:19.

Zhang, X., Sagiya, T., 2018. Intraplate strike-slip faulting, stress accumulation, and shear localization of a crust-upper mantle system with nonlinear viscoelastic material. J. Geophys. Res.: Solid Earth 123 (10), 9269–9285.